Near-Surface Salinity Reveals the Oceanic Sources of Moisture for Australian Precipitation through Atmospheric Moisture Transport

SAURABH RATHORE

Institute for Marine and Antarctic Studies, University of Tasmania, and ARC Centre of Excellence for Climate System Science, Hobart, Tasmania, Australia

NATHANIEL L. BINDOFF

Institute for Marine and Antarctic Studies, University of Tasmania, and ARC Centre of Excellence for Climate Extremes, and CSIRO Oceans and Atmosphere, and Australian Antarctic Program Partnership, Hobart, Tasmania, Australia

CAROLINE C. UMMENHOFER

Woods Hole Oceanographic Institution, Woods Hole, Massachusetts, and ARC Centre of Excellence for Climate Extremes, Sydney, New South Wales, Australia

HELEN E. PHILLIPS

Institute for Marine and Antarctic Studies, University of Tasmania, and ARC Centre of Excellence for Climate Extremes, Hobart, Tasmania, Australia

MING FENG

CSIRO Oceans and Atmosphere, Indian Ocean Marine Research Centre, Crawley, Western Australia, and Centre for Southern Hemisphere Oceans Research, CSIRO, Hobart, Tasmania, Australia

(Manuscript received 31 July 2019, in final form 12 May 2020)

ABSTRACT

The long-term trend of sea surface salinity (SSS) reveals an intensification of the global hydrological cycle due to human-induced climate change. This study demonstrates that SSS variability can also be used as a measure of terrestrial precipitation on interseasonal to interannual time scales, and to locate the source of moisture. Seasonal composites during El Niño–Southern Oscillation/Indian Ocean dipole (ENSO/IOD) events are used to understand the variations of moisture transport and precipitation over Australia, and their association with SSS variability. As ENSO/IOD events evolve, patterns of positive or negative SSS anomaly emerge in the Indo-Pacific warm pool region and are accompanied by atmospheric moisture transport anomalies toward Australia. During co-occurring La Niña and negative IOD events, salty anomalies around the Maritime Continent (north of Australia) indicate freshwater export and are associated with a significant moisture transport that converges over Australia to create anomalous wet conditions. In contrast, during co-occurring El Niño and positive IOD events, a moisture transport divergence anomaly over Australia results in anomalous dry conditions. The relationship between SSS and atmospheric moisture transport also holds for pure ENSO/IOD events but varies in magnitude and spatial pattern. The significant pattern correlation between the moisture flux divergence and SSS anomaly during the ENSO/IOD events highlights the associated ocean–atmosphere coupling. A case study of the extreme hydroclimatic events of Australia (e.g., the 2010/11 Brisbane flood) demonstrates that the changes in SSS occur before the peak of ENSO/IOD events. This raises the prospect that tracking of SSS variability could aid the prediction of Australian rainfall.

Corresponding author: Saurabh Rathore, saurabh.rathore@utas.edu.au

DOI: 10.1175/JCLI-D-19-0579.1

1. Introduction

The water cycle is an integral part of the climate system that regulates the temperature of our planet by maintaining the balance between energy and mass via evaporation, condensation, and precipitation processes (Bowen 2011). The presence of water vapor in Earth's atmosphere serves as a greenhouse gas, and its distribution is subjected to climate change (Raval and Ramanathan 1989; Bindoff et al. 2013). Due to the effect of anthropogenic climate change, the water cycle has intensified over the past few decades, and some of the best evidence for this intensification is in the long-term ocean salinity measurements (Huntington 2006; Helm et al. 2010; Durack et al. 2012). The intensification of the global water cycle on long time scales follows the paradigm ''rich-gets-richer and the poor-gets-poorer,'' which means wet regions are getting wetter and dry regions are getting drier (Trenberth 2011). However, some studies (Greve et al. 2014; Kumar et al. 2015; Feng and Zhang 2016; Polson and Hegerl 2017) show that the wet-gets-wetter and dry-gets-drier paradigm has discrepancies on regional and short temporal scales between the expected response of the hydrological cycle to global warming and observed changes over land. While the ocean salinity patterns reflect the intensified global water cycle (Helm et al. 2010; Durack et al. 2012), it also serves the purpose of nature's rain gauge (Yu 2011) and is an effective tool to estimate global evaporation E and precipitation P changes (Hosoda et al. 2009).

In the context of using regional SSS as nature's rain gauge, its links with the terrestrial precipitation are also gaining attention and raising the prospects of using SSS as a precursor for terrestrial precipitation (Li et al. 2016a,b; Chen et al. 2019). Examples are the assimilation of SSS in coupled models to improve rainfall predictions (through the improvement of the upper ocean thermal structure) (Yaremchuk 2006; Koul et al. 2018; Seelanki et al. 2018). Moreover, SSS also plays an active role in the development of ENSO and IOD events and aids in improving the forecast of these events (Zhu et al. 2014; Hackert et al. 2019; Sun et al. 2019).

Various studies show the effect of SST and large-scale atmospheric circulation anomalies on Australian rainfall during ENSO/IOD events (Ashok et al. 2003; Cai et al. 2009; Ummenhofer et al. 2009, 2011; Taschetto et al. 2011; King et al. 2015) but the link between SSS and the moisture transport during these events from the adjacent ocean basins has not been addressed. In this study, we demonstrate that variations in the SSS across the Indo-Pacific warm pool region on interannual time scales are profoundly linked with the moisture transport over Australia. In particular, we use a composite analysis of SSS, Australian precipitation, and convergence/divergence of atmospheric moisture during the ENSO/IOD events to demonstrate these linkages.

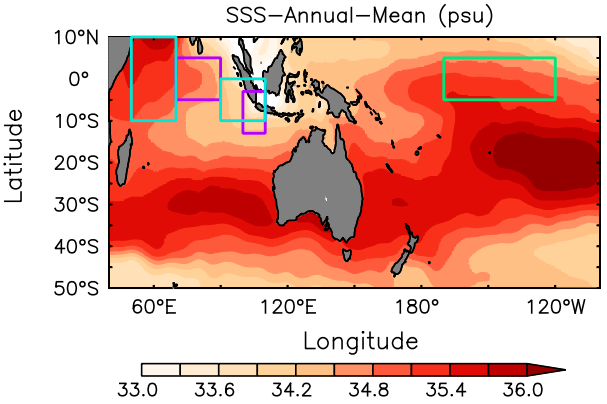

FIG. 1. Annual mean of sea surface salinity (SSS) for the study area overlaid with the boxes for the dipole mode index (DMI; cyan), salinity dipole index (purple), and Niño-3.4 index (green).

An application of these linkages is demonstrated for the case of an extreme hydroclimatic event in Australia during 2010/11 austral summer that brought one of the worst floods on record to Brisbane with 35 deaths and estimated damage to be more than $2 billion (NCCARF 2011; Holmes 2012; Hayes and Goonetilleke 2013; Queenland Government 2015). The year of 2010/11 was a co-occurring La Niña and negative IOD event, which generally brings high rainfall to northeast Australia (Evans and Boyer-Souchet 2012); a drop of 5 mm in global mean sea level also resulted from this event (Boening et al. 2012; Fasullo et al. 2013; Lim and Hendon 2015).

2. Data and methodology

a. Data

We focus our analyses on the Indo-Pacific region 40°E–100°W, 50°S–10°N (i.e., the domain shown in Fig. 1). Monthly means of oceanic and atmospheric parameters from 1961 to 2017 are used from various observational and reanalysis products. To assess the interseasonal to interannual climate variability, we used the Niño-3.4 index for ENSO and the dipole mode index (DMI) for IOD. The ENSO index is the area average SST anomaly bounded by the region 5°S–5°N, 170°–120°W and based on the monthly time series of ERSSTv5 (Huang et al. 2017). The DMI is based on Saji et al. (1999) and represents the SST anomaly difference between the western equatorial (50°–70°E, 10°S–10°N) and the southeastern equatorial (90°–110°E, 10°S–0°N) the Indian Ocean. Both indices were linearly detrended for further analysis to focus on interseasonal to interannual climate

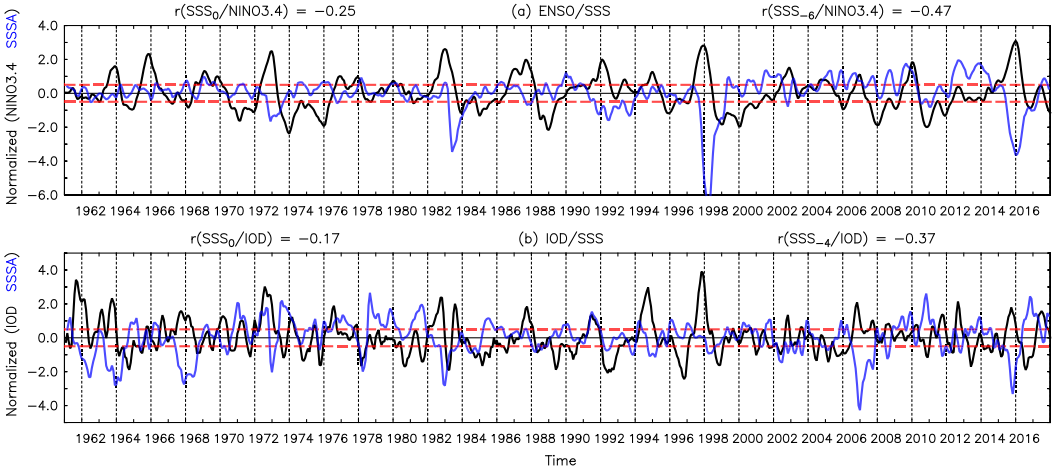

FIG. 2. Monthly normalized time series of (a) the El Niño–Southern Oscillation (ENSO) index of the Niño-3.4 region (170°–120°W, 5°S–5°N) (black) and SSS anomaly averaged over the Niño-3.4 region (blue) and (b) the Indian Ocean dipole (IOD) index (black) and the dipole index of SSS anomaly (blue), which is the difference of the central equatorial Indian Ocean (70°–90°E, 5°S–5°N) and the region off the Sumatra/Java coast (100°–110°E, 13°–3°S). The red dashed line indicates the threshold of ±0.5 standard deviation of the Niño-3.4 index and DMI. The correlation cofficient r at zero lead/lag between the SSS anomaly and the Niño-3.4 index (SSS_0/$Niño_{3.4}$) is −0.25 and for the SSS anomaly dipole and IOD index (SSS_0/IOD) is −0.17. Similarly, the lead/lag correlation shows that the SSS anomaly lags Niño-3.4 index by 6 months (SSS_{-6}/$Niño_{3.4}$) with maximum r of −0.47 and lags IOD index by 4 months (SSS_{-4}/IOD) with maximum r of −0.37. All of the correlation coefficients are statistically significant at 95% from a two-tailed Student's t test.

variability. The sources for the monthly time series data of the ENSO index and DMI are https://origin.cpc.ncep.noaa.gov/products/analysis_monitoring/ensostuff/ONI_v5.php and https://www.esrl.noaa.gov/psd/gcos_wgsp/Timeseries/DMI/.

We used monthly values of specific humidity and horizontal winds between 1000 and 500 hPa and surface wind components from NCEP–NCAR Reanalysis 1 (Kalnay et al. 1996).

Monthly SST data are from HadISST1 (Rayner et al. 2003), and monthly SSS data is from Hadley Centre subsurface objective analyses (EN 4.2.1) (Gouretski and Reseghetti 2010; Good et al. 2013). Terrestrial precipitation data over Australia is from the Australian Water Availability Project (AWAP) (Raupach et al. 2009).

Analyses shown in the results section were repeated with different observational and reanalysis products which include SSS from ORAS4 (Balmaseda et al. 2013), SST from ERSSTV5 (Huang et al. 2017), terrestrial precipitation from Climate Research Unit (CRU) (New et al. 2000), zonal and meridional winds and specific humidity between 1000 and 500 hPa from ERA-Interim (Dee et al. 2011). Results were qualitatively similar and are not shown here.

b. Methods

The seasonal composite from the anomaly fields of SST, 10-m surface winds, SSS, moisture flux divergence (MFD), and its divergent component and Australian precipitation has been constructed for years of ENSO and IOD events. The years of ENSO and IOD events were selected using the seasonally averaged time series of the ENSO index and DMI during November–February (NDJF) and August–November (ASON), respectively.

To include a maximum number of significant events in the composite fields, we select years where the index in question (seasonally averaged time series) exceeds a threshold of ±0.5 standard deviation of the respective long-term time series (Lestari and Koh 2016) (Fig. 2). The choice of other thresholds, e.g., ±0.7 or ±1.0 standard deviation, does not cause any significant change in the results. The years that satisfy this criterion in the seasonally averaged time series of NDJF for ENSO and ASON for DMI are chosen and further divided into six categories, as shown in Table 1. These categories are pure El Niño, pure La Niña, pure positive IOD, pure negative IOD, co-occurring El Niño and positive IOD, and co-occurring La Niña and negative IOD events. Most of the ENSO and IOD years, classified by our study into different categories agree with previous studies (Saji and Yamagata 2003; Meyers et al. 2007; Ummenhofer et al. 2011; Pepler et al. 2014), and also with the years identified by the Bureau of Meteorology and the National Weather Service Climate Prediction Center (Table 1). The results from co-occurring events are shown in the main

TABLE 1. ENSO and IOD events in six categories with their respective years from 1961 to 2017 based on the methodology adopted in this study. Symbols are as follows: an asterisk (*) indicates years similar to Meyers et al. (2007) and Ummenhofer et al. (2011), $^{+}$ indicates years similar to Bureau of Meteorology, Australia, $^{\#}$ indicates years similar to Saji and Yamagata (2003), $^{\$}$ indicates years similar to Pepler et al. (2014), and $^{@}$ indicates ENSO years similar to the National Weather Service Climate Prediction Center.

Event category	Years of occurrence
Pure El Niño	1965/66$^{*+\#\$@}$, 1969/70$^{+\#\$@}$, 1979/80$^{@}$, 1986/87$^{*\#@}$, 2004/05$^{*@}$, 2009/10$^{+\$@}$, 2014/15$^{+@}$
Pure La Niña	1985/86$^{*\#}$, 1988/89$^{*+\#\$@}$, 1995/96$^{@}$, 1999/2000$\$^{@}$, 2000/01$^{@}$, 2008/09$^{+\$@}$
Pure positive IOD	1961$^{*+\#\$}$, 1966, 2012$^{+\$}$
Pure negative IOD	1980*, 1981*$^{+}$, 1992$^{*+\#\$}$, 2001
Co-occurring El Niño and positive IOD	1963/64$^{*+\#@}$, 1972/73$^{*+\#\$@}$, 1976/77$^{@}$, 1977/78$^{\$@}$, 1982/83$^{*+\#\$@}$, 1987/88$^{@}$, 1991/92$^{*@}$, 1994/95$^{+\$@}$, 1997/98$^{*+\#\$@}$, 2002/03$^{@}$, 2006/07$^{+\$@}$, 2015/16$^{+@}$
Co-occurring La Niña and negative IOD	1964/65$^{+\#\$@}$, 1970/71$^{@}$, 1971/72$^{\#\$@}$, 1973/74$^{@}$, 1974/75$^{@}$, 1975/76$^{*+\#\$@}$, 1984/85$^{@}$, 1996/97$^{\#}$, 1998/99$^{+@}$, 2005/06$^{@}$, 2010/11$^{+\$@}$, 2016/17$^{@}$

text and the remaining pure events in the auxiliary information.

The computation of MFD is carried out by using Eq. (1):

$$\mathrm{MFD} = \left(\frac{1}{g}\right)\nabla \cdot \int_0^{P_s} q\mathbf{V}\, dp \cong (E - P), \qquad (1)$$

where MFD is the moisture flux divergence, g is the gravitational acceleration (9.8 m s^{-2}), q is specific humidity (g kg^{-1}), $\mathbf{V}$ is horizontal wind velocity (m s^{-1}), E is evaporation, and P is precipitation. Moisture flux $q\mathbf{V}$ is computed at each pressure level of the reanalysis and then integrated from the surface (1000 hPa) to 500 hPa. The upper limit of integration is taken as 500 hPa, as the majority of moisture in the atmosphere is concentrated below that level, as suggested by previous studies (Zhou and Yu 2005; Li et al. 2013; Seager and Henderson 2013; Li et al. 2016b). The divergent component of moisture flux (MF) is computed by solving Poisson equations (Lynch 1988). The transport and divergent component of moisture flux together show the pathway of atmospheric moisture that directly link the oceanic sources of moisture with the terrestrial sink regions.

For significance testing of the composite analysis, we use Hotelling's T-square test (Hotelling 1931). The null hypothesis is that the composite mean (μ_1) = long-term seasonal mean (μ_2). The number of composite samples is equal to the number of ENSO and IOD events in each category; the number of seasonal mean samples is 57 (i.e., the total number of years in the reanalysis time series). The test statistic for Hotelling's T-square test is shown in Eq. (2); see also appendix A for more detail.

$$T = \frac{(\overline{\mu_1} - \overline{\mu_2})}{\sqrt{S^2_{\mathrm{pool}}\left(\frac{1}{n_1} + \frac{1}{n_2}\right)}}, \quad S^2_{\mathrm{pool}} = \frac{(n_1 - 1)S_1^2 + (n_2 - 1)S_2^2}{n_1 + n_1 - 2}. \qquad (2)$$

The null hypothesis will be rejected at $\alpha/2$ significance level when $T \geq t_{n_1+n_2-2,\,\alpha/2}$ with $n_1 + n_1 - 2$ degrees of freedom.

We also performed a linear correlation for the relationship between SSS and MFD during co-occurring ENSO and IOD events. In the interest of conciseness, results are only shown for co-occurring ENSO and IOD events in the subsequent subsections.

3. SST and SSS in the Niño-3.4 and DMI regions

The relationship between ENSO/IOD events and SSS can be established by examining the monthly time series of various standard ENSO and DMI indices and SSS in the study region. Figure 2a shows the monthly time series of the Niño-3.4 index, and the SSS anomaly averaged over the Niño-3.4 region and Fig. 2b for the DMI and the SSS dipole mode. The SSS dipole mode is defined as the difference of SSS anomaly averaged over the central equatorial Indian Ocean (70°–90°E, 5°S–5°N) and the region off the Sumatra and Java coast (100°–110°E, 13°–3°S) (J. Li et al. 2016). The main advantage of using the SSS dipole mode index is for detecting and characterizing its relationship with the SST anomaly dipole and providing positive feedback to the formation of the IOD events (J. Li et al. 2016; Sun et al. 2019).

The correlation between the SSS and SST anomaly over the Niño-3.4 region is −0.25 at zero lag but the correlation increases to −0.47 (significant at 95% confidence) when the Niño-3.4 index leads the SSS anomaly by 6 months (Fig. 2a). This result is consistent with Ballabrera-Poy et al. (2002) and Singh and Delcroix (2011), where they show that the signal of ENSO in SSS lags the ENSO signal in SST by 3–6 months. Moreover, this negative correlation exists between the Niño-3.4 SST, and equatorial SSS anomalies is due to the increase of local rainfall and anomalous eastward advection of low-salinity warm pool waters in the equatorial band

associated with El Niño (Ballabrera-Poy et al. 2002; Singh and Delcroix 2011).

Zhu et al. (2014) and Hackert et al. (2019) also suggested that the SSS significantly contributes to the surface dynamics of the western and south-central Pacific to trigger ENSO events. According to Ballabrera-Poy et al. (2002), Hackert et al. (2011, 2019), Zhu et al. (2014), Zhao et al. (2016), and Zhi et al. (2019), fresh anomalies advected from the Southern Hemisphere to the western equatorial region through subduction processes lead to increased barrier layer thickness and a shoaling of mixed layer depth (MLD). Fresh anomalies at the surface reduce mixing, decrease buoyancy, and shoal the thermocline, thus enhancing the Kelvin wave amplification, which leads to more efficient air–sea ENSO coupling. Moreover, Hackert et al. (2019) show that by improving near-surface density structure via SSS assimilation in coupled models, ENSO forecasts are improved with respect to observed Niño-3.4 SST anomalies for both the temporal (i.e., correlation) and amplitude [root-mean-square difference (RMSD)] signals and particularly for the 2–10-month lead times.

The correlation of SSS anomaly with DMI at zero lead/lag −0.17 and increases to −0.37 when DMI leads the SSS anomaly by four months (Fig. 2b). Previous studies (J. Li et al. 2016; Kido and Tozuka 2017; Kido et al. 2019; Sun et al. 2019) suggest that the SSS anomalies due to evaporation, precipitation, zonal advection by winds and mesoscale eddies impact the development of IOD events.

4. Climatological conditions over the Indo-Pacific

In the seasonal cycle, there are clear associations between ocean salinity and atmospheric moisture fluxes. The seasonal climatology of SSS, SST, Australian precipitation, MFD, and the divergent component of moisture flux is shown in Fig. 3. From MAM (March–May) to DJF (December–February), the relatively high (low) SSS around 20°–40°S (10°N–10°S) is in good agreement with divergence (convergence) of moisture over the ocean (Fig. 3, all panels). The divergence of moisture leaves an imprint of increased SSS whereas the convergence of moisture leaves an imprint of freshened SSS in the ocean. The region of high SSS (Fig. 3, first column) around Australia and in the tropical Pacific between 150°E and 100°W shows the oceanic source of atmospheric moisture associated with MFD (Fig. 3, second column). Similarly, the low SSS (Fig. 3, first column) of the intertropical convergence zone (ITCZ) and South Pacific convergence zone (SPCZ) is indicative of the convergence of atmospheric moisture (Fig. 3, second column). The Indian Ocean off western Australia and the Pacific Ocean off eastern Australia are the primary sources of moisture supply (Fig. 3, second column) for the mean Australian precipitation. The moisture originating from the Indo-Pacific Ocean converges over land, as shown by the vectors of the divergent component of moisture flux and high precipitation on the northwestern, northeastern, southwestern, southeastern, and east coasts of Australia (Fig. 3, third column).

This analysis shows that the atmospheric moisture originating from the ocean leaves an imprint on SSS and this atmospheric moisture converges over Australia where it can precipitate. Hence, from the climatological perspective, the Indian and the Pacific Oceans adjacent to Australia are the main sources of moisture for mean Australian precipitation, and the mean SSS signal is a robust indicator of this atmospheric moisture transport. However, the maxima and minima of MFD are displaced with respect to the maxima and minima of SSS (Fig. 3, cf. columns 1 and 2), which warrants further investigation. Moreover, during climactic events (e.g., ENSO and IOD), the conditions vary considerably from the mean state.

5. Evolution of the SSS signature during co-occurring ENSO and IOD events with links for Australian precipitation

In this section, we show the link between Australian precipitation and SSS signatures during co-occurring ENSO/IOD events. We focus here on these types of events because they have the strongest signal for demonstrating the relationship between precipitation and SSS. In co-occurring events, IOD peaks in strength during SON and is generally followed by ENSO that peaks during DJF. A positive IOD (pIOD) event is followed by El Niño, and negative IOD (nIOD) is followed by La Niña; this sequence/combination is known as a co-occurring event. Based on this sequence there are 12 co-occurring El Niño and pIOD events (1963/64, 1972/73, 1976/77, 1977/78, 1982/83, 1987/88, 1991/92, 1994/95, 1997/98, 2002/03, 2006/07, and 2015/16) and 12 co-occurring La Niña and nIOD events (1964/65, 1970/71, 1971/72, 1973/74, 1974/75, 1975/76, 1984/85, 1996/97, 1998/99, 2005/06, 2010/11, and 2016/17) (Table 1). However, the independence of ENSO and the IOD is still debated (Allan et al. 2001; Meyers et al. 2007; Stuecker et al. 2017).

a. Co-occurring El Niño and positive IOD event

In co-occurring El Niño and pIOD events, anomalously warm SST anomalies appear in the equatorial Pacific during boreal summer (JJA). The Indian Ocean shows a pIOD signature starting from JJA, peaking in

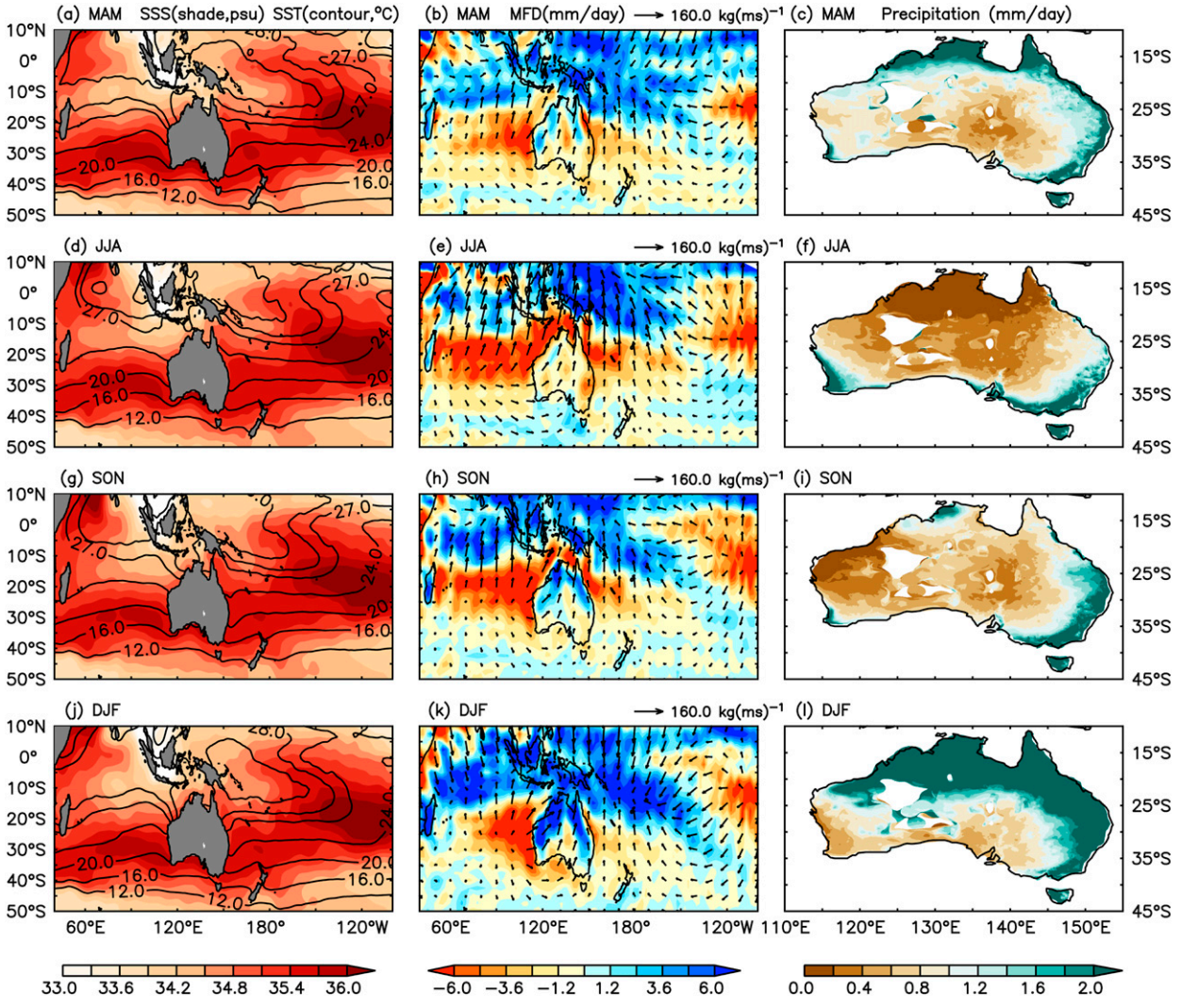

FIG. 3. Seasonal climatology of (a),(d),(g),(j) sea surface salinity (SSS; shaded) overlaid by SST (contoured), (b),(e),(h),(k) moisture flux divergence (shaded) where positive indicates convergence and negative indicates divergence overlaid by the divergent component of moisture flux (vectors), and (c),(f),(i),(l) precipitation over Australia.

SON, and dissipating in DJF (i.e., the season when ENSO peaks) (Fig. 4, first column). During these events, surface winds show significant coherence with the SST anomaly pattern. The intensification of the anomalous easterlies off the Java/Sumatra coast in the Indian Ocean during SON coincides with the SST anomaly pattern of pIOD. Similarly, the relaxation of easterlies over the equatorial Pacific coincides with the El Niño–related SST anomaly pattern (Fig. 4, first column).

The anomalous SSS anomaly pattern (Fig. 4, second column) around northern Australia starts evolving prior to the peak seasons of ENSO and IOD. The SSS anomaly signature appears during the boreal spring and peaks progressively with the ENSO and IOD events. During these events, the region of positive SSS anomaly around northern Australia exhibits large-scale patterns of salinification, whereas the equatorial Indian and the Pacific Ocean, away from the Maritime Continent, exhibit freshening (Fig. 4, second column). This pattern in SSS, to a large extent, reflects the enhanced evaporation and precipitation associated with the co-occurring ENSO/IOD events across the Indo-Pacific. This pattern of SSS anomaly is also reflected in MFD. MFD is taken to be a proxy for total precipitable water present in the atmospheric column (Fig. 4, third column).

Positive MFD reflects the convergence of moisture, and negative MFD reflects the divergence. The MFD signature in the atmosphere evolves simultaneously with the SSS anomaly in the ocean. The divergence (convergence) of moisture flux generally coincides with a

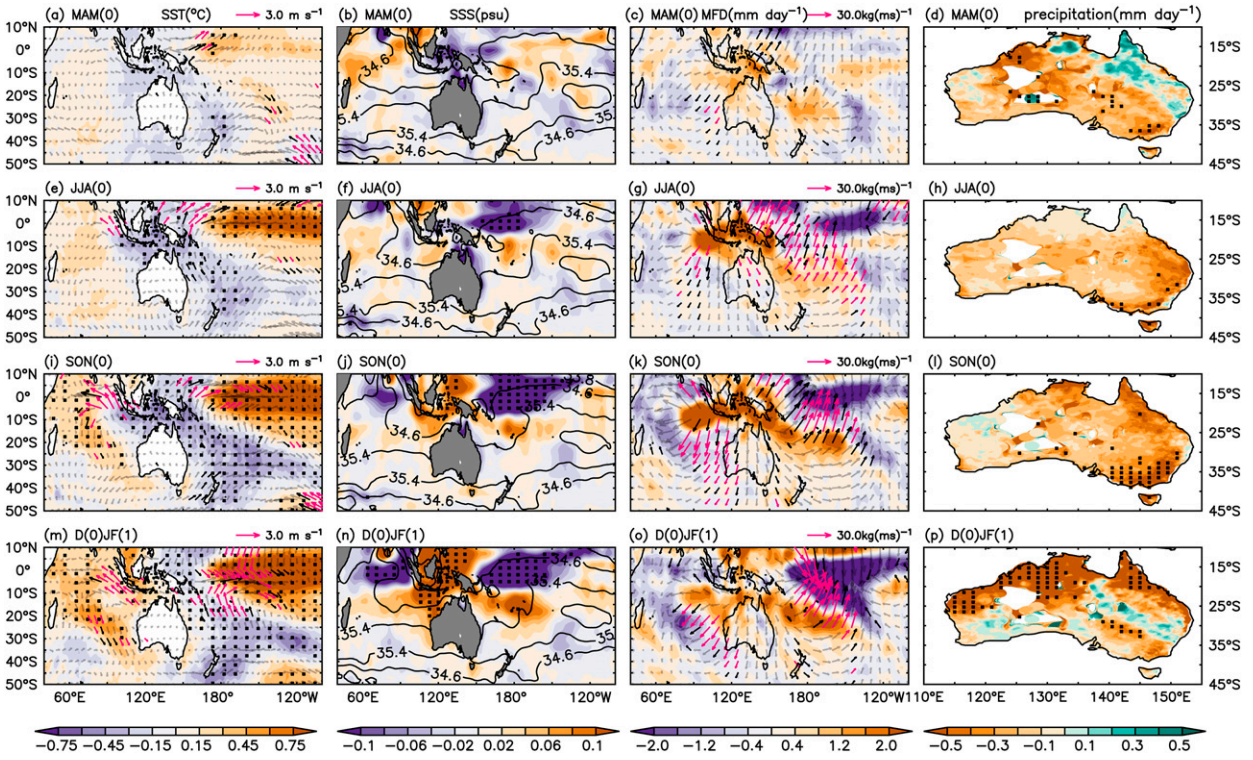

FIG. 4. Seasonal composite mean during co-occurring El Niño and pIOD of (a),(e),(i),(m) SST anomaly (shaded; °C) overlaid by 10-m anomalous surface winds (vectors; m s^{-1}), (b),(f),(j),(n) sea surface salinity (SSS) anomaly (shaded; psu) overlaid by seasonal climatology of SSS (contour), (c),(g),(k),(o) moisture flux divergence anomaly (MFD; mm day^{-1}; shaded) overlaid by the divergent component of moisture flux anomaly (kg m^{-1} s^{-1}; vectors), and (d),(h),(l),(p) Australian precipitation anomaly (mm day^{-1}). Black dots indicate regions that are statistically significant at 95%, thick black vectors are statistically significant at 90%, and thick magenta vectors are statistically significant at 95% from Hotelling's *T*-square test.

positive (negative) SSS anomaly signature. During co-occurring El Niño/pIOD, the divergence of moisture flux evolves over northern Australia and becomes more organized as pIOD and El Niño peak in SON and DJF, respectively. A large part of the atmospheric moisture originates and is transported from the Indonesian seas and SPCZ region, as shown by the vectors of the divergent component of moisture flux (Fig. 4, third column). The vectors of the divergent component of moisture flux show the pathways of moisture transport.

The divergence and convergence of moisture over land are as important as those over the ocean because they indicate the increased likelihood for terrestrial precipitation. During co-occurring El Niño and pIOD event, the mean moisture supply toward Australia is weakened by an anomalous reversal of the direction of moisture flux (Fig. 4, third column). The reduced mean moisture transport coincides with the divergence over the Australian continent and is thus less likely to precipitate during co-occurring El Niño and pIOD events. During these events, weak convergence of moisture is present over southern Australia (Fig. 4o), which is associated with an increase in precipitation over the same region during DJF (Fig. 4p). In contrast, the strong divergence over northern Australia (Fig. 4o) associated with negative rainfall anomalies (Fig. 4p) coincides with the strong subsidence over northern Australia and anomalously dry conditions (Taschetto et al. 2011).

The co-occurring El Niño and pIOD brings strong anomalous dry conditions over Australia (Fig. 4, fourth column) because the moisture originating from the ocean encounters strong divergence over land. The weak convergence over western and central Australia during JJA shows relatively less dry conditions as compared to southeastern Australia (Fig. 4h). As pIOD and El Niño evolve and peak in SON and DJF, respectively, the magnitude of moisture transport anomaly becomes intensified. During SON (Fig. 4k), western Australia receives significant moisture transport from the Indian Ocean and coincides with a weak convergence of moisture. In contrast, the moisture transport from the Pacific Ocean coincides with divergence from eastern to central Australia (Fig. 4k). This results in moderately wet conditions over western Australia and significant

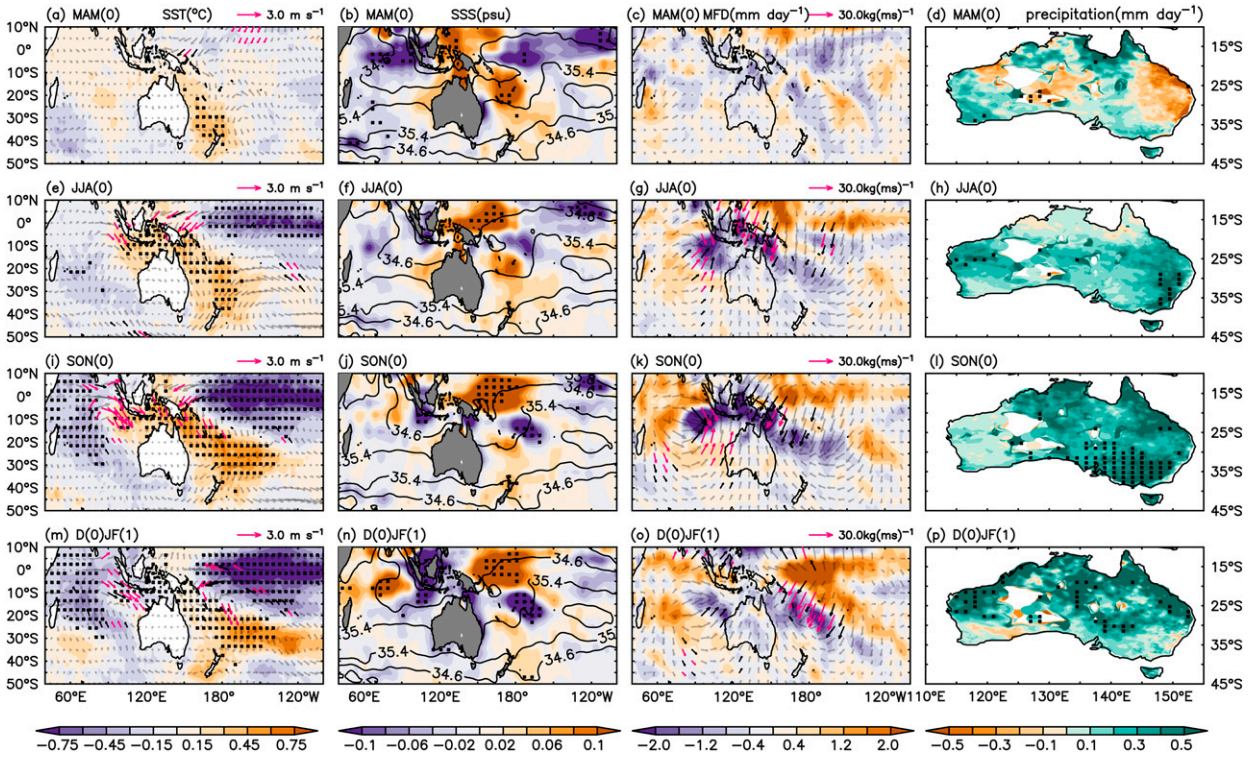

FIG. 5. Seasonal composite mean during co-occurring La Niña and nIOD of (a),(e),(i),(m) sea surface temperature anomaly (SST anomaly; shaded; °C) overlaid by 10-m anomalous surface winds (vectors; m s^{-1}), (b),(f),(j),(n) sea surface salinity anomaly (SSS anomaly; shaded; psu) overlaid by seasonal climatology of sea surface salinity (SSS; contour), (c),(g),(k),(o) moisture flux divergence anomaly (MFD; mm day^{-1}; shaded) overlaid by the divergent component of moisture flux anomaly (kg m^{-1} s^{-1}; vectors), and (d),(h),(l),(p) Australian precipitation anomaly (mm day^{-1}). Black dots indicate regions that are statistically significant at 95%, thick black vectors are statistically significant at 90%, and thick magenta vectors are statistically significant at 95% from Hotelling's *T*-square test.

drying over the rest of Australia (Fig. 4l). In the boreal winter season DJF (Fig. 4o), the moisture transport from the Indian and the Pacific Ocean coincides with weak convergence (strong divergence) over southern (northern) Australia. This results in weak positive precipitation anomalies in southern Australia and significant dry anomalies over northern Australia (Fig. 4p).

This overall suppression of rainfall over Australia during co-occurring El Niño and pIOD events is likely to be due to a tropical and extratropical teleconnection, triggered by the diabatic heating anomalies and Rossby wave trains (Cai et al. 2011).

Our analysis (Fig. 4) suggests that the exchange of moisture between ocean and atmosphere leaves a distinct signature in SSS on the ocean, earlier than the peak SST anomalies during El Niño and pIOD events (e.g., Figs. 2 and 4) and that these patterns can be traced through the atmospheric moisture pathway.

b. Co-occurring La Niña and negative IOD event

The following analysis of co-occurring La Niña and nIOD also reveals these same relationships but of opposite sign (Fig. 5). During co-occurring La Niña and nIOD events, a negative SST anomaly developed in the equatorial Pacific Ocean during boreal summer (JJA) and peaks in boreal winter (DJF). While in the Indian Ocean, the nIOD peaks in SON, as shown in Fig. 5 (first column). The anomalous SST condition is supported by the intensification of westerlies in the equatorial Indian Ocean and easterlies in the equatorial Pacific during SON and DJF, respectively.

During the development of La Niña and nIOD events, a significant positive anomaly of SSS evolves in the equatorial Indian and Pacific Oceans between 10°S and 10°N during MAM (Fig. 5b), off the Maritime Continent. Similarly, another positive anomaly of SSS over 10°–30°S, 170°E–150°W is also observed. As the co-occurring La Niña and nIOD evolve, the region around northern Australia gets fresher whereas the region of the Indian and the Pacific Ocean off the Maritime Continent gets saltier (Fig. 5, second column).

Similarly, the atmospheric moisture is divergent over the region of positive SSS anomaly and convergent over the negative SSS anomaly (i.e., fresher region) (Fig. 5,

third column). During JJA, a significant amount of moisture moves toward the Australian continent from two branches connected to the Pacific Ocean (Fig. 5g). The first branch is a direct route crossing northeast Australia from the equatorial Pacific, as shown by Brown et al. (2009). The second branch crosses southeast Australia over the Tasman Sea. Both branches coincide with weak convergence over Australia, and this is reflected in enhanced rainfall over Australia (Fig. 5h). In the following season (SON), both the Indian and the Pacific Ocean contribute moisture transport toward Australia (Fig. 5k). During this season, there is a three-way moisture supply that includes the two branches from the Pacific Ocean, as described above, and an additional branch from the Indian Ocean toward southwestern Australia. Similar conditions prevail in DJF with further intensification and widespread convergence of moisture over the Australian continent (Fig. 5o). This suggests that the SSS anomaly is organized by the atmospheric circulation and reflects the regions dominated by evaporation and precipitation during co-occurring La Niña and nIOD events.

Australian precipitation progressively increases from JJA to DJF during co-occurring La Niña and nIOD (Fig. 5, fourth column), due to enhanced mean moisture supply toward Australia. This anomalous transport of moisture from the Indian and the Pacific Ocean experiences strong convergence over the Australian continent and is likely to precipitate. The anomalously wet condition over Australia during co-occurring La Niña and nIOD events is likely to be associated with the moisture convergence due to lower surface pressure and cyclonic anomalies from the barotropic Rossby wave trains that emanate from the tropical Indian Ocean (McBride and Nicholls 1983; Meyers et al. 2007; Cai et al. 2011; Lim et al. 2016). These wet conditions contrast with the situation during co-occurring El Niño and pIOD events when conditions over Australia are anomalously dry. The conditions during co-occurring La Niña and nIOD events bring a significant amount of rain, and the origin of moisture that feeds the precipitation is evident in the SSS anomaly in the prior season.

The analyses for the remaining categories (i.e., pure El Niño, pure La Niña, pure pIOD, and pure nIOD) are shown in the appendices (see Figs. B1–B4). It is worth mentioning that the magnitude of anomalies generated by pure ENSO and IOD events (Figs. B1–B4) are weak compared to co-occurring ENSO and IOD events (Figs. 4 and 5). The underlying mechanism for this contrast, which involves the ENSO and IOD dynamics, is explained by previous studies (Meyers et al. 2007; Risbey et al. 2009; Ummenhofer et al. 2009, 2011; Cai et al. 2011).

6. Relationship between moisture flux divergence and SSS anomaly

In the previous section, we have described the oceanic and atmospheric links between SSS anomaly and MFD during co-occurring ENSO and IOD events. In this section, we demonstrate the statistical relationship between SSS anomaly and MFD and show the evolution of the signal throughout the event. The seasonal evolution of the relationship between SSS anomaly and MFD in the Indian and Pacific Ocean for each co-occurring event is obtained from the pattern correlation.

Prior to pattern correlation analysis, we masked and regridded the MFD field to the $1° \times 1°$ spatial resolution of the SSS anomaly field. We then normalized these fields by their respective spatial standard deviation to provide a comparable contribution from each field at each grid point. Each point of the scatterplot of the pattern present in the normalized SSS anomaly and MFD field corresponds to the value of the SSS anomaly and MFD field at the same grid point (Fig. 6).

The coupling between SSS anomaly and MFD is primarily tested over the tropical region of the Indian (60°–120°E, 30°S–10°N) and Pacific Oceans (150°E–150°W, 30°S–10°N) where a strong signal is present.

a. Pacific Ocean during co-occurring ENSO and IOD events

The evolution of ocean–atmosphere coupling between the SSS anomaly and MFD in the Pacific Ocean during co-occurring ENSO/IOD events is shown in Figs. 6a–d. As ENSO predominantly influences the Pacific Ocean, the pattern correlation between the SSS anomaly and MFD during co-occurring El Niño and pIOD events progressively strengthens from MAM to DJF. Similar behavior in the correlation is also observed for co-occurring La Niña and nIOD events except in JJA when the correlation is slightly weaker (0.31) compared to 0.36 in MAM. The maximum correlation is observed during DJF (i.e., when ENSO peaks), with 0.64 and 0.46 for co-occurring El Niño/pIOD and co-occurring La Niña/nIOD events respectively and significant at 95% confidence (Fig. 6d). The strengthening of coupling between the SSS anomaly and MFD anomaly from MAM to DJF shows the enhancement of the signal from the weak developing state of ENSO and IOD to the strong mature state. The progressive increment in correlation from MAM to DJF (Figs. 6a–d) also shows the organization and synchronization of ocean–atmosphere coupling during these large-scale climatic fluctuations. This represents the signal of SSS anomaly intensifying with the convergence/divergence of moisture in the atmosphere.

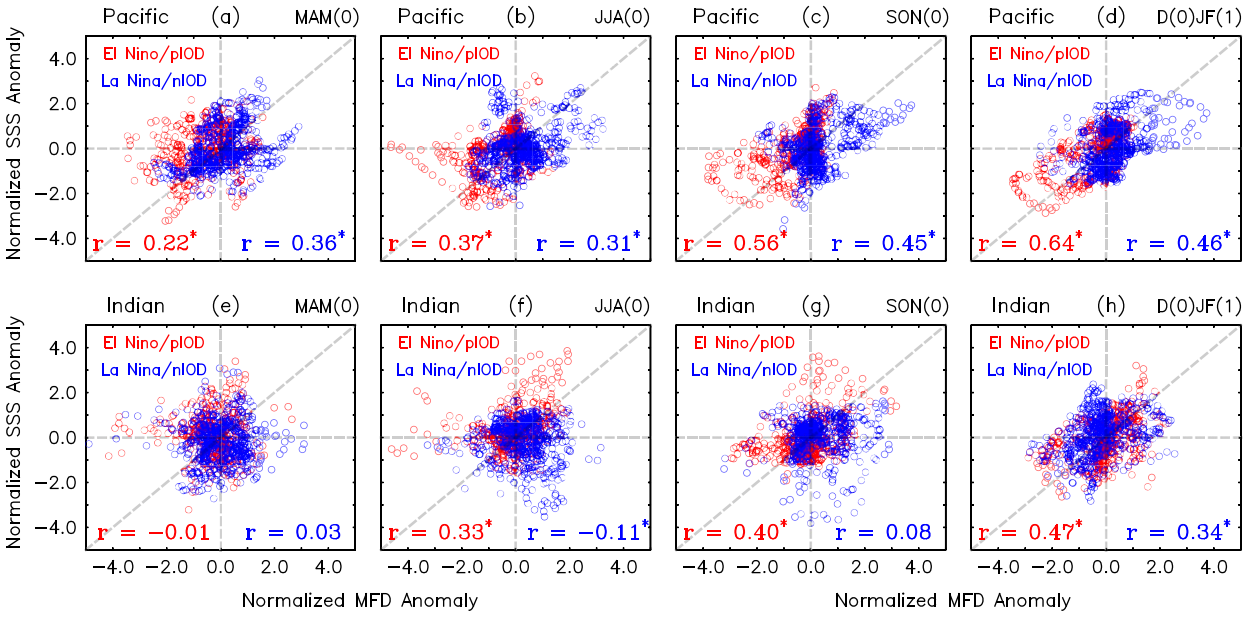

FIG. 6. Pattern correlation analysis of seasonal composite mean of spatially normalized SSS anomaly and MFD anomaly with their respective standard deviation during co-occurring El Niño and pIOD (red) and co-occurring La Niña and nIOD (blue) over the (a)–(d) Pacific (150°E–150°W, 30°S–10°N) and (e)–(h) Indian Ocean (60°–120°E, 30°S–10°N). The pattern correlation coefficient r is shown at the bottom in all panels. The correlation coefficients that are statistically significant at 95% from a two-tailed Student's t test are marked with asterisks.

b. *Indian Ocean during co-occurring ENSO and IOD events*

The Indian Ocean also shows a strengthening of the pattern correlation from MAM to DJF (Figs. 6e–h) as both ENSO and IOD influence it. However, the effect of ENSO on the Indian Ocean lasts longer than the IOD when the anomalous dipole mode pattern of SST anomaly during SON vanishes in DJF and turns into basinwide warming. During co-occurring El Niño and pIOD events, maximum correlation is observed during DJF (0.47) at 95% confidence. However, during the co-occurring La Niña and nIOD event, DJF has a maximum correlation of 0.34 significant at 95% as compared to the previous seasons but lower than for the co-occurring El Niño and pIOD events. This asymmetrical correlation is plausibly the combined effect of the co-occurring ENSO and IOD events and the asymmetry in the ENSO events (Hong et al. 2010).

It is important to note that the spread of the correlation pattern is reduced considerably in the Pacific Ocean from MAM to DJF. In the Indian Ocean, the spread is large in all seasons except in DJF, when it is more aligned along the best fit line. This observation suggests that in the Pacific Ocean the ocean–atmosphere coupling evolves with the ENSO events, while in the Indian Ocean this coupling is weak (Jansen et al. 2009). Figure 6 also shows that the correlation coefficient for the co-occurring El Niño and pIOD events is greater than that for La Niña and nIOD events in both the Indian and the Pacific Ocean. One possible reason for this is the positive skewness of the ENSO and IOD events; that is, the anomalies generated by the co-occurring El Niño and pIOD events are larger in magnitude than the co-occurring La Niña and nIOD (Hong et al. 2010; Cai et al. 2012).

This correlation analysis (Fig. 6), along with Figs. 4 and 5, corroborates the relationship between the SSS and the precipitation over Australia via atmospheric moisture transport. It is important to note that the correlation analysis (Fig. 6) has no consideration of the lead/lag component at this stage. However, when incorporating a lead of 1 month to the SSS anomaly with respect to the MFD anomaly, the correlation is marginally improved in most of the seasons in both events (Fig. B5). This suggests that the relationship between SSS and the MFD could be improved with the consideration of some moderate lead/lag associated with these fields.

7. Case study of Australian hydroclimatic extremes in 2010/11

The previous sections make the case that SSS is a useful ocean variable for understanding precipitation over Australia. Here we look more closely at the utility

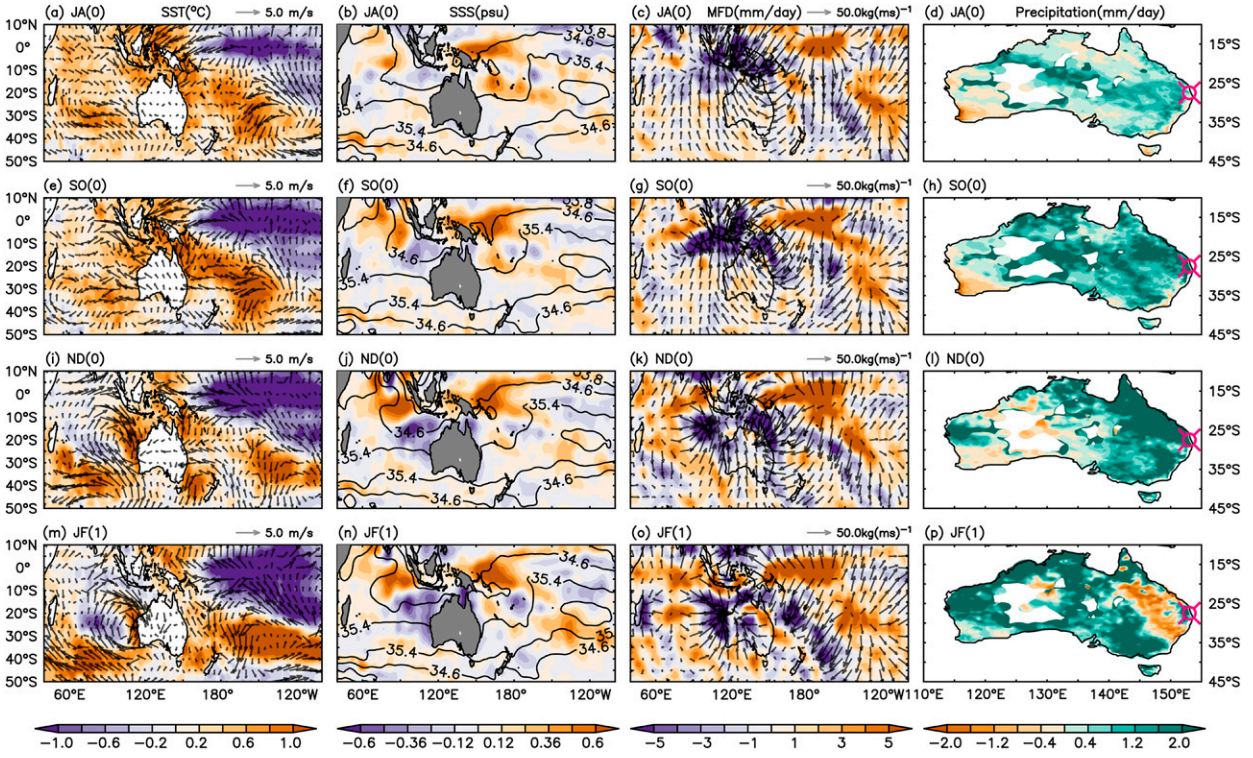

FIG. 7. Case study of 2010/11 extreme hydroclimatic events of Australia (Brisbane flood), during a co-occurring La Niña and nIOD event. Bimonthly means from July–August 2010 to January–February 2011 of (a),(e),(i),(m) sea surface temperature anomaly (SST anomaly; shaded; °C) overlaid by 10-m surface winds (vectors; m s^{-1}), (b),(f),(j),(n) sea surface salinity anomaly (SSS anomaly; shaded; psu) overlaid by seasonal climatology of sea surface salinity (SSS; contour), (c),(g),(k),(o) moisture flux divergence anomaly (MFD; mm day^{-1}; shaded) overlaid by the divergent component of moisture flux anomaly (kg m^{-1} s^{-1}; vectors), and (d),(h),(l),(p) Australian precipitation anomaly (mm day^{-1}). Here, the red circle is the location of Brisbane, which was severely affected by this flood event.

of SSS for the extreme hydroclimatic events in Australia. In particular, the flooding event in Brisbane and southern Queensland happened during the co-occurring La Niña and nIOD events of 2010/11. This case study serves the purpose of exploring the role of SSS anomaly over the Indo-Pacific region as a precursor for enormous moisture export for extreme precipitation events.

During this co-occurring La Niña and nIOD event, a strong SST anomaly developed in the eastern tropical Indian Ocean near the island of Java/Sumatra and the equatorial Pacific Ocean, as shown by the bimonthly evolution maps (Fig. 7, first column). The SST anomaly in the Indian Ocean shows a strong nIOD pattern during November–December (Fig. 7i). Similarly, the anomalous cooling of the equatorial Pacific Ocean during July–August (Fig. 7a) peaks during November–February (Figs. 7i,m). The signatures of the SST anomaly pattern are aligned with the surface wind anomaly (Fig. 7, first column) and indicate the intensification of westerlies (easterlies) over the eastern tropical Indian (equatorial Pacific) Ocean. At the same time, a positive SSS anomaly organizes in the equatorial (5°S–5°N) Indian and Pacific Ocean (Indo-Pacific warm pool) and also in the extratropical region of the Indian (60°–110°E, 30°–40°S) and the Pacific Ocean (100°–170°W, 20°–40°S), showing intense evaporation during the co-occurring La Niña and nIOD event (Fig. 7, second column). The development of intense anomalous freshening (negative SSS anomaly) is also apparent around the western coast of Australia and is an indication of more intense precipitation perhaps associated with strong Indonesian Throughflow (ITF) (Feng et al. 2015).

During the co-occurring La Niña and nIOD event of 2010/11, a large amount of moisture originates from the Pacific Ocean in July–August and is transported toward the Australian continent (Fig. 7, third column). It is observed that during this event, there are four branches supplying moisture that converge over eastern Australia (Fig. 7, third column). The first branch of moisture is over northeast Australia and has a pathway that comes directly from the equatorial Pacific. The second branch converges over southeast Australia and originates from the extratropical Pacific over the Tasman Sea. The third branch of moisture shows convergence over western

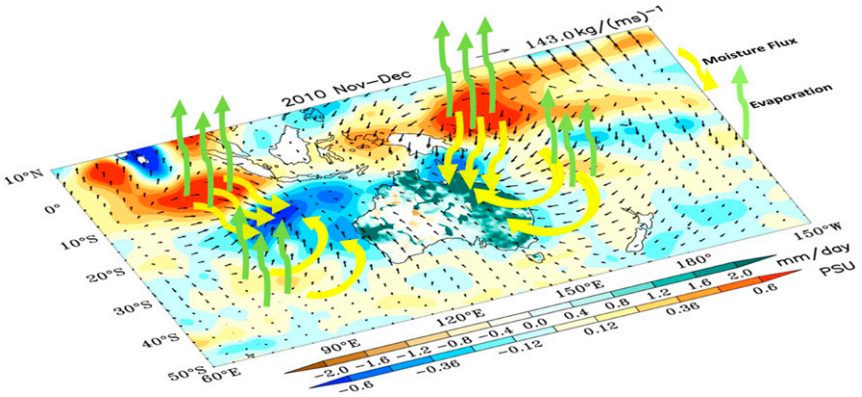

FIG. 8. Schematic illustration of the extreme hydroclimatic events of Australia during November–December 2010 (Brisbane floods in eastern Australia). The presence of a high-salinity signal in the Indian and Pacific Oceans around 10°S–10°N shows a region of high evaporation. This extra moisture (green arrows) is transported toward the region indicating freshening in the ocean and the Australian landmass as shown by the vectors of atmospheric moisture transport (yellow arrows). In this figure the moisture transported from the high salinity region in the Indian Ocean converges over the ocean to the northwest of Australia, whereas the moisture transported from the high salinity region of Pacific Ocean converges over the east coast of Australia.

Australia and originates from the eastern tropical Indian Ocean. The fourth branch of moisture transport emerges during November–February (Figs. 7k,o), from the extratropical southeastern Indian Ocean. The anomalously high supply of moisture from this branch directly converges over the west coast of Australia (Figs. 7k,o) and also causes a freshening in the adjacent eastern Indian Ocean (Figs. 7j,n).

The emergence of the moisture transport corresponds with the positive SSS anomaly, which is apparent in the prior season and intensifies with the evolution of the co-occurring La Niña and nIOD event. Moreover, the convergence of the first, second, and third branches of moisture supply is associated with the effect of La Niña and nIOD as shown by previous studies (Risbey et al. 2009; Ummenhofer et al. 2009; Cai et al. 2011). However, the substantial moisture convergence and freshening on the west coast of Australia coincide with the Ningaloo Niño and the co-occurring La Niña and nIOD event. During Ningaloo Niño, the Leeuwin Current intensified, and the west coast of Australia experienced anomalously warm SST and intensification of surface winds (Figs. 7i,m) (Feng et al. 2013; Pearce and Feng 2013; Kataoka et al. 2014).

The combination of events (i.e., co-occurring La Niña and nIOD with Ningaloo Niño) draws anomalously high moisture that converges over the Australian continent and results in heavy precipitation. A large part of the moisture comes from the Pacific Ocean and causes heavy precipitation over the east coast of Australia (Figs. 7l,p and 8) and, in particular, across southern Queensland. Similarly, the precipitation over western Australia is driven by moisture transport from the Indian Ocean (Figs. 7l,p and 8). This study shows that the source of moisture for intense precipitation over Australia emerges in the ocean in prior seasons with anomalously high positive SSS anomaly. The suggested role of long-term ocean warming in contributing to the severity of the Queensland floods event during 2010/11 (Ummenhofer et al. 2015) is consistent with a local intensification of the hydrological cycle, as evidenced by the strong SSS signal shown here.

8. The relative contributions of the Indian and the Pacific Ocean toward Australian rainfall

The relative contributions of the Indian and the Pacific Ocean to moisture transport over Australia are shown in Fig. 9 for all seasons during mean climatological conditions and co-occurring ENSO and IOD events. Here, the net moisture transport (given in Sv; 1 Sv = 10^6 m^3 s^{-1}) is the spatial integration of MFD (mm day^{-1}) over the continental area of Australia (Fig. 9). In the mean climatology conditions during DJF (Fig. 9j), the moisture transport of 0.074 Sv (31% of the net moisture transport) is over western Australia, showing that the Indian Ocean is the primary source of mean moisture supply for the west coast of Australia. However, the Pacific Ocean, adjacent to the east coast of Australia, has a transport of 0.054 Sv (Fig. 9j), which represents 22% of the net moisture transport over Australia. Eastern and

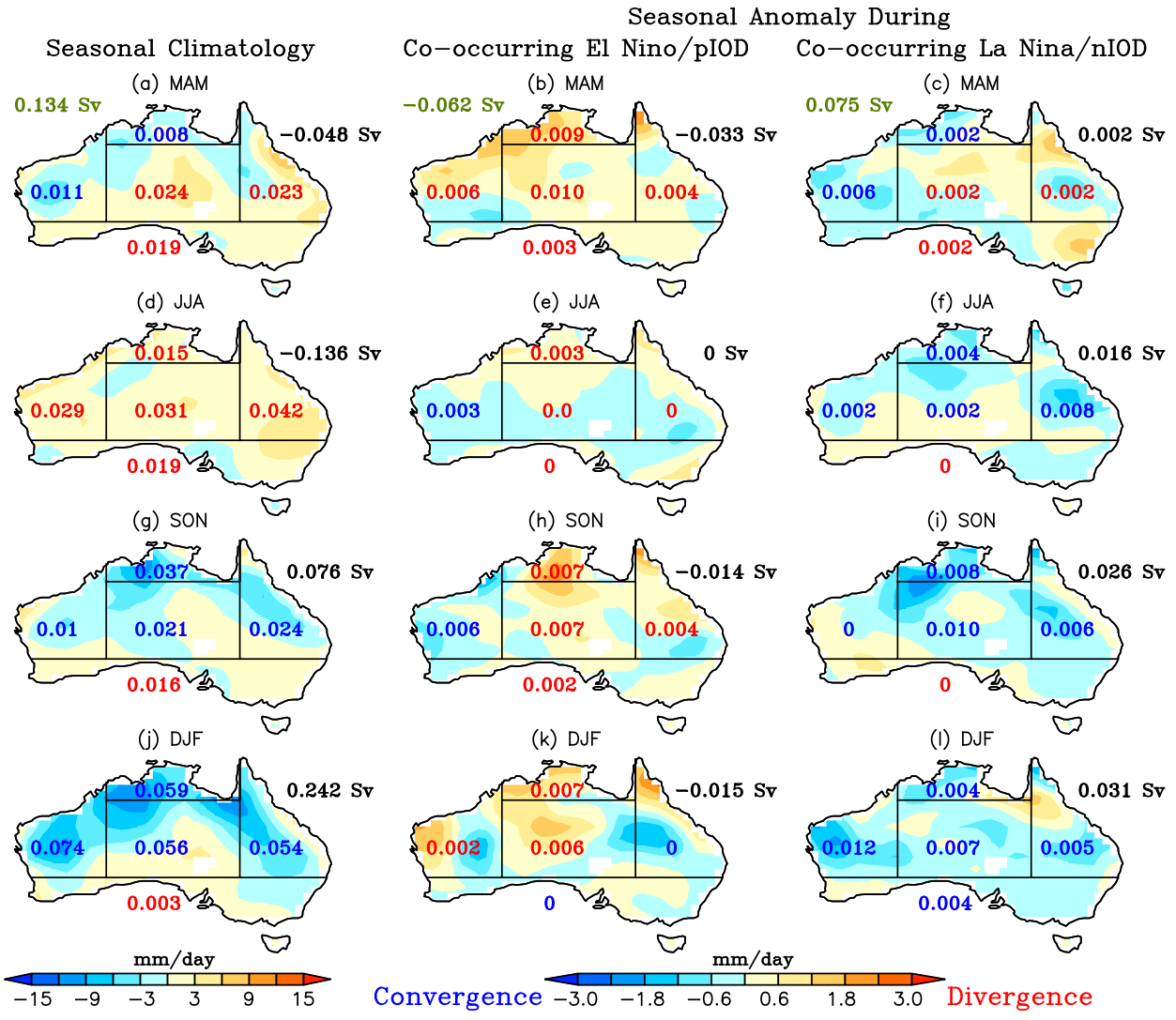

FIG. 9. Spatially integrated moisture flux divergence (Sv; 1 Sv = 10^6 m^3 s^{-1}) over the Australian continent for western (113°–125°E, 15°–31°S), northern (125°–142°E, 11°–18°S), eastern (142°–154°E, 11°–31°S), southern (113°–154°E, 31°–44°S), and central (125°–142°E, 18°–31°S) Australia during MAM, JJA, SON, and DJF for (a),(d),(g),(j) climatology, (b),(e),(h),(k) co-occurring El Niño and pIOD, and (c),(f),(i),(l) co-occurring La Niña and nIOD. Here shading indicates vertically integrated moisture flux divergence (mm day^{-1}) in which blue is convergence and orange is divergence with the magnitude in blue and red (numbers) for net converged and diverged moisture transport (Sv) in the box, respectively. Here black numbers indicate net moisture transport (Sv) for each season over Australia where positive (negative) is convergence (divergence), and the green numbers show the net annual converging/diverging moisture transport (Sv) for seasonal climatology, co-occurring El Niño and pIOD, and co-occurring La Niña and nIOD.

western Australia combined result in 53% of the net moisture transport from the Pacific and the Indian Ocean. The remaining 47% of moisture can be attributed to the transport toward northern Australia from the Southern Ocean sector (Fig. 3k) and also local recycling.

In contrast, during co-occurring El Niño and pIOD events, the whole of Australia is anomalously dry due to the high divergence of moisture in all seasons. In JJA (0.003 Sv) and SON (0.006 Sv), western Australia experiences a weak convergence of atmospheric moisture, which is supplied by the Indian Ocean from north of 30°S (Fig. 4). During the co-occurring La Niña and nIOD event, there is an anomalously high convergence of moisture over the Australian landmass (Fig. 9): the Indian (Pacific) Ocean is the primary source of moisture over western (eastern) Australia during DJF (JJA and SON) (Fig. 5). The anomalous moisture transport by the Indian and the Pacific Ocean during the DJF season of co-occurring La Niña and nIOD events is 0.012 Sv (i.e., 39%) and 0.005 Sv (i.e., 16%) of the net moisture

transport over Australia with associated convergence (Fig. 9l).

This analysis shows that the tropical Indian Ocean on the western coast and the tropical Pacific Ocean on the eastern coast of Australia are the primary source regions for the moisture supply. It is worth mentioning that the southern sector of the Indian Ocean also contributes to the mean and anomalous (La Niña and nIOD event) transport of moisture toward the Australian landmass (Figs. 3 and 5).

9. Discussion

Previous studies have concentrated on the changes in SST during ENSO and IOD events for monitoring or anticipating terrestrial precipitation anomalies. This study brings a new perspective on the link between SSS and Australian precipitation via pathways of atmospheric moisture transport during these events. A composite analysis is carried out for the ENSO and IOD events to establish the link between SSS anomalies and Australian precipitation. The resultant maps included here demonstrate that the high- and low-SSS regions are associated with convergence and divergence of the atmospheric moisture flux. The pattern of positive SSS anomaly during ENSO and IOD events provides an insight into the oceanic sources of moisture transport toward Australia. However, the MFD variations in the atmosphere are not perfectly aligned with the SSS anomaly signals in the ocean. The correlation between SSS and MFD anomalies is likely to be further improved by accounting for oceanic advection. We would expect the oceanic advection anomalies associated with surface wind variations to be the primary source of difference in longer-term pattern correlations along with the temporal lead/lag, as evidenced by the displaced maxima of MFD and SSS anomalies in the seasonal climatology (e.g., Figs. 3a,b).

This study shows that the anomalous moisture transport during ENSO and IOD events significantly affects the mean moisture transport toward land from the adjacent ocean basins. The anomalous moisture transport during co-occurring El Niño and pIOD (La Niña and nIOD) events oppose (reinforces) the mean moisture transport. The effect from co-occurring ENSO and IOD events (Figs. 4 and 5) is more intense than the pure events (Figs. B1–B4). In a broad sense, the combined effect of ENSO and the IOD on Australian rainfall is generally more extreme than either on its own (Risbey et al. 2009). During co-occurring El Niño and pIOD events, we find the ocean north of Australia supplies a large amount of moisture, which is associated with the positive SSS anomaly there. However, the strong atmospheric subsidence over Australia makes it less likely to precipitate over the land (Taschetto et al. 2011).

In contrast, during the La Niña event, the moisture transport associated with the positive SSS anomaly in the Indo-Pacific warm pool region coincides with strong atmospheric convergence over land, resulting in anomalously wet conditions over Australia. In the case of pure events, the anomalies generated by the ENSO events (Figs. B1 and B2) have a stronger hydrological response than the IOD events (Figs. B3 and B4). This suggests that among the large-scale drivers for Australian rainfall, ENSO is the key player at interannual time scales that has broad influence and impact, both on the ocean and atmosphere (Risbey et al. 2009).

Our results also suggest that changes that occur in the SSS of the preceding season are associated with the convergence and divergence of atmospheric moisture during the development of ENSO and IOD events (e.g., Figs. 4 and 5). These changes in the SSS are also observed in the case study of the extreme hydroclimatic events in eastern Australia that resulted in the 2010/11 Brisbane floods (Fig. 7). This result shows that the organization of moisture transport is well captured by the changes in SSS. The emergence of an SSS anomaly signature in the preceding season, and its intensification in subsequent seasons (Figs. 4 and 5), suggests that SSS can be used as a potential predictor for terrestrial rainfall over Australia. The potential use of SSS as a precursor for terrestrial precipitation has also been demonstrated for the Sahel and the U.S. Midwest region (Li et al. 2016a,b).

Some preliminary analysis of Australian rainfall prediction using SSS is shown in Fig. B5 and Fig. 10. Figure B5, similar to Fig. 6, shows a slight improvement in the correlation when the SSS anomaly leads MFD by one month. Further, the leading mode of empirical orthogonal function (EOF1) of Australian rainfall during DJF shows that the rainfall is highly distributed over northern Australia and extends southeastward (Fig. 10a) with an explained variance of 32%.

Similarly, the EOF1 of SSS in the preceding season (i.e., SON; Fig. 10b), shows strong loading of SSS in the western Pacific warm pool region (150°E–160°W, 10°S–10°N), which is strengthened in the concurrent season (i.e., DJF; Fig. 10c), suggesting the signature of ENSO development. The variance explained by the EOF1 of SON and DJF SSS is 18.56% and 19.23% respectively. The regression of the principal component time series (PC1) associated with the EOF1 of (SON and DJF) SSS with the MFD and the divergent component of moisture flux (vectors) is shown in Figs. 10b and 10c, respectively. The regression pattern of significant moisture transport toward Australia originates in the prior season (SON)

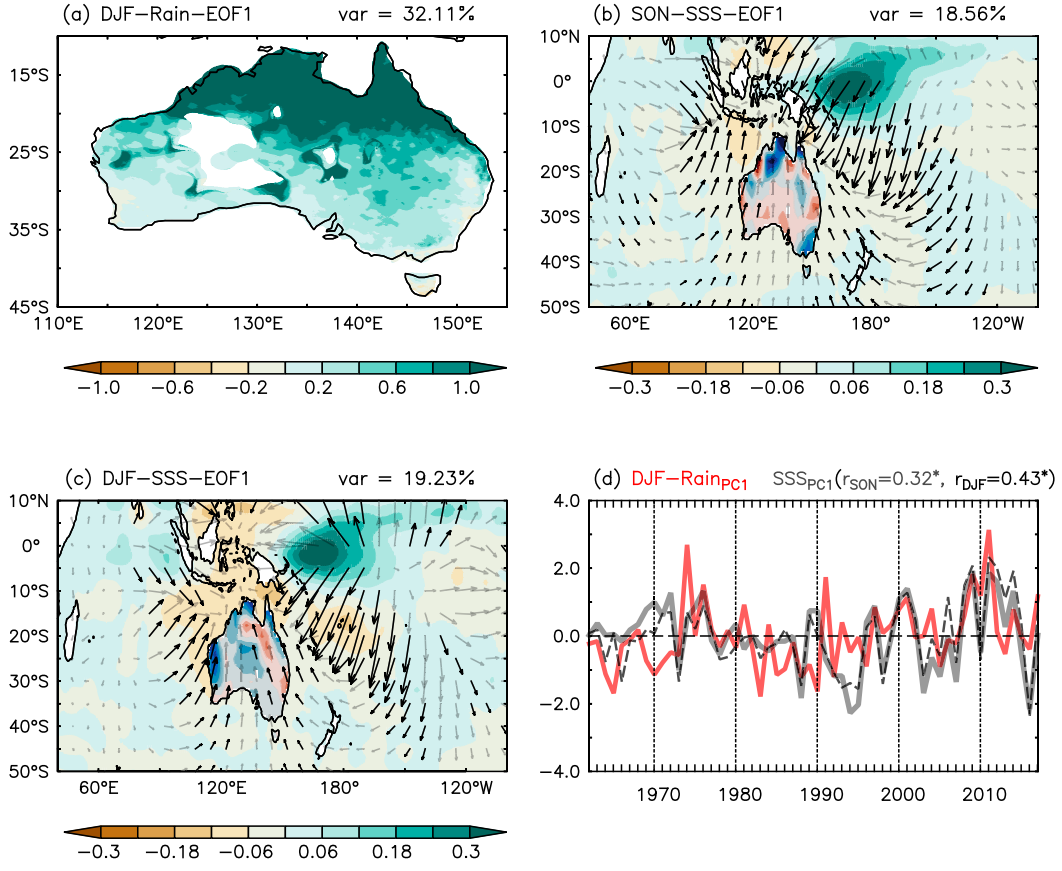

FIG. 10. Leading mode of empirical orthogonal function (EOF1) of (a) DJF rainfall over Australia and (b) SON SSS over the whole domain (40°E–100°W, 50°S–10°N) overlaid by the vectors of moisture transport estimated from the regression of divergent component of moisture flux of SON onto the leading principal component (PC1) associated with the EOF1 of SON SSS; the colored field over Australia is the regressed pattern of SON MFD onto the PC1 of SON SSS where blue and red represents convergence and divergence respectively. (c) As in (b), but for DJF SSS, DJF moisture transport vectors, and DJF MFD. (d) Normalized PC1 time series of DJF rainfall (red), SON SSS (gray thick), and DJF SSS (black dashed). The correlation coefficients r_{SON} and r_{DJF} represent the correlation between the PC1 of DJF rainfall and the SSS anomaly of SON and DJF; respectively. Asterisks (thick black vectors) indicate the statistical significance of correlation coefficient and (regression) at 95% from a two-tailed Student's *t* test.

and becomes more intense in the concurrent season (DJF). This moisture transport (Figs. 10b,c) is associated with the SSS loading and converges/diverges over Australia, resembling the ENSO and IOD pattern, as shown in Figs. 4 and 5. This analysis suggests that the positive (negative) loading of SSS in the Indo-Pacific warm pool region is associated with the La Niña and nIOD (El Niño and pIOD) event and hence the convergence (divergence) of moisture transport toward land. These results show a clear path of atmospheric moisture transport originates from the Indo-Pacific warm pool toward Australia at these times.

The signatures of ENSO and IOD events are also apparent in the SSS anomaly, as shown in Fig. 2 and also in Fig. B6, which shows that a modest, yet significant, anticorrelation exists between them. The correlation between the PC1 of the SSS anomaly for the study region (40°E–100°W, 50°S–10°N) and the Niño-3.4 index is −0.65 (significant at 95% confidence) and is −0.40 (significant at 95% confidence) in the case of DMI during the SON season.

It is also worth mentioning the diversity present within the ENSO events, as discussed by Santoso et al. (2017). They show that the extreme El Niño event of 2015/16 has distinct features as compared to previous extreme El Niño events of 1982/83 and 1997/98. During the El Niño event of 2015/16 record-breaking warm SST anomalies were present in the central Pacific, whereas in 1982/83 and 1997/98 SST anomalies peak toward the far eastern Pacific. Moreover, the 2015/16 El Niño corresponds to

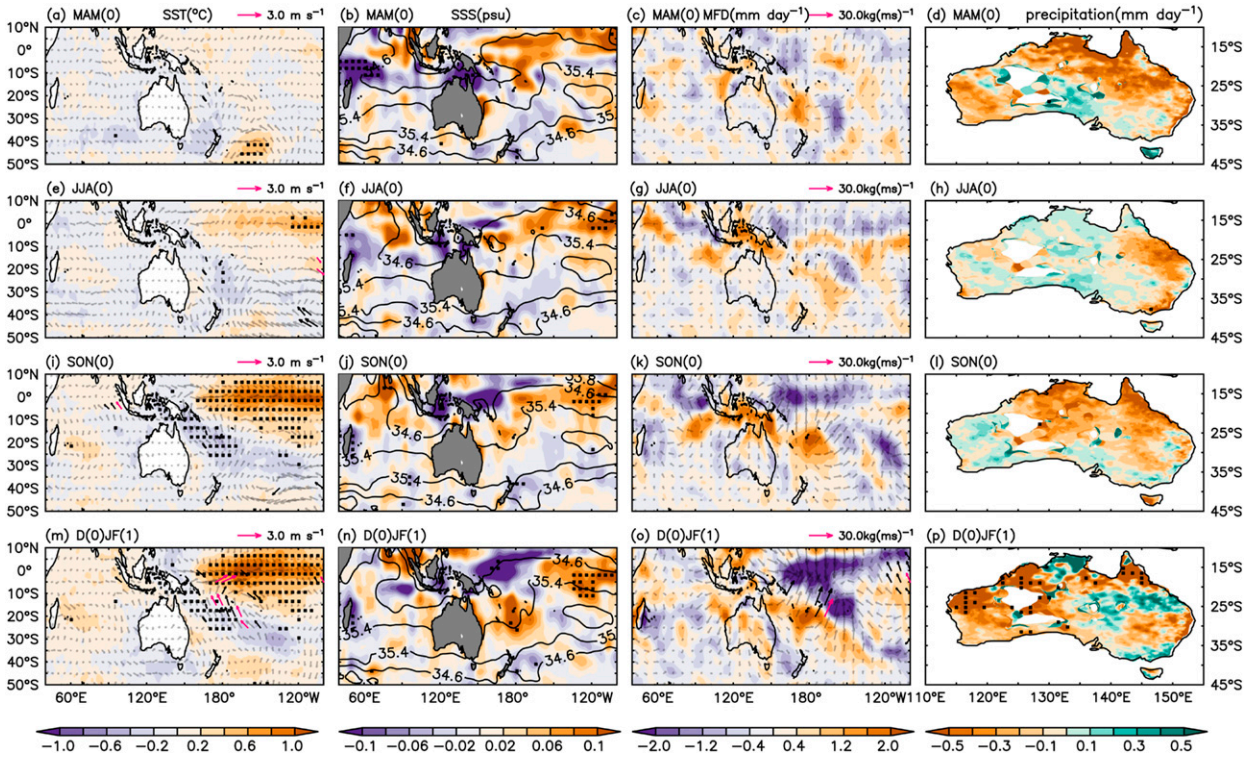

FIG. B1. Seasonal composite mean during pure El Niño of (a),(e),(i),(m) sea surface temperature anomaly (SST anomaly; shaded; °C) overlaid by 10-m anomalous surface winds (vectors; m s^{-1}), (b),(f),(j),(n) sea surface salinity anomaly (SSS anomaly; shaded; psu) overlaid by seasonal climatology of sea surface salinity (SSS, contour), (c),(g),(k),(o) moisture flux divergence anomaly (MFD; mm day^{-1}; shaded) overlaid by the divergent component of moisture flux anomaly (kg m^{-1} s^{-1}; vectors), and (d),(h),(l),(p) Australian precipitation anomaly (mm day^{-1}). Black dots indicate regions that are statistically significant at 95%, thick black vectors are statistically significant at 90%, and thick magenta vectors are statistically significant at 95% from Hotelling's *T*-square test.

heavy rainfall in the Niño-4 region (160°E–150°W and 5°S–5°N) as compared to the 1982/83 and 1997/98 events, which showed intense precipitation over the eastern equatorial Pacific (Niño-3 region; 150°–90°W, 5°S–5°N). Similarly, the extreme La Niña event of 1998/99 is different than the subsequent La Niña of 1999/2000. The former one starts from an extremely warm condition associated with the 1997/98 El Niño and thus requires a significantly large cooling to get started, whereas the latter one does not require further cooling. This shows the diversity within the ENSO events (Santoso et al. 2017). Such diversity can also be seen with the IOD events co-occurring with the ENSO events in which extreme El Niño events have occurred with notable pIODs (e.g., 2015/16). In contrast, extreme La Niña events were accompanied by neutral and weak IODs (Santoso et al. 2017). Therefore, by taking the ENSO/IOD diversity (e.g., eastern and central Pacific ENSO) into account, the relationship between SSS and rainfall over land can be further improved.

It is worth mentioning that the moisture originates in the prior season (SON) and leaves an imprint on the SSS and contributes to the terrestrial precipitation over Australia in the following season (DJF). This relationship can be further inferred from the correlation analysis between the PC1 of DJF rainfall and the (SON and DJF) SSS (Fig. 10d). A significant correlation ($r = 0.32$ at 95% confidence) exists between the PC1 of DJF rainfall and the PC1 of SON SSS, which further increased to 0.43 when both the fields are from the concurrent season (DJF). This analysis suggests that there is a significant link between DJF rainfall of Australia and the SSS through atmospheric moisture transport. This analysis warrants further investigation about the oceanic source regions (anomalously high SSS regions), for atmospheric moisture, that can be used for the prediction of Australian rainfall.

The land surface processes during ENSO and IOD events also affect the precipitation and convergence/divergence of atmospheric moisture (Evans et al. 2011, 2017; Decker et al. 2015; Holgate et al. 2019; Zhao et al. 2019). The large-scale dynamics translate into local land surface processes that are influenced by vegetation, soil moisture, irrigation, orography, and so on. Furthermore, due to the uncertainty in estimating $E - P$ (evaporation

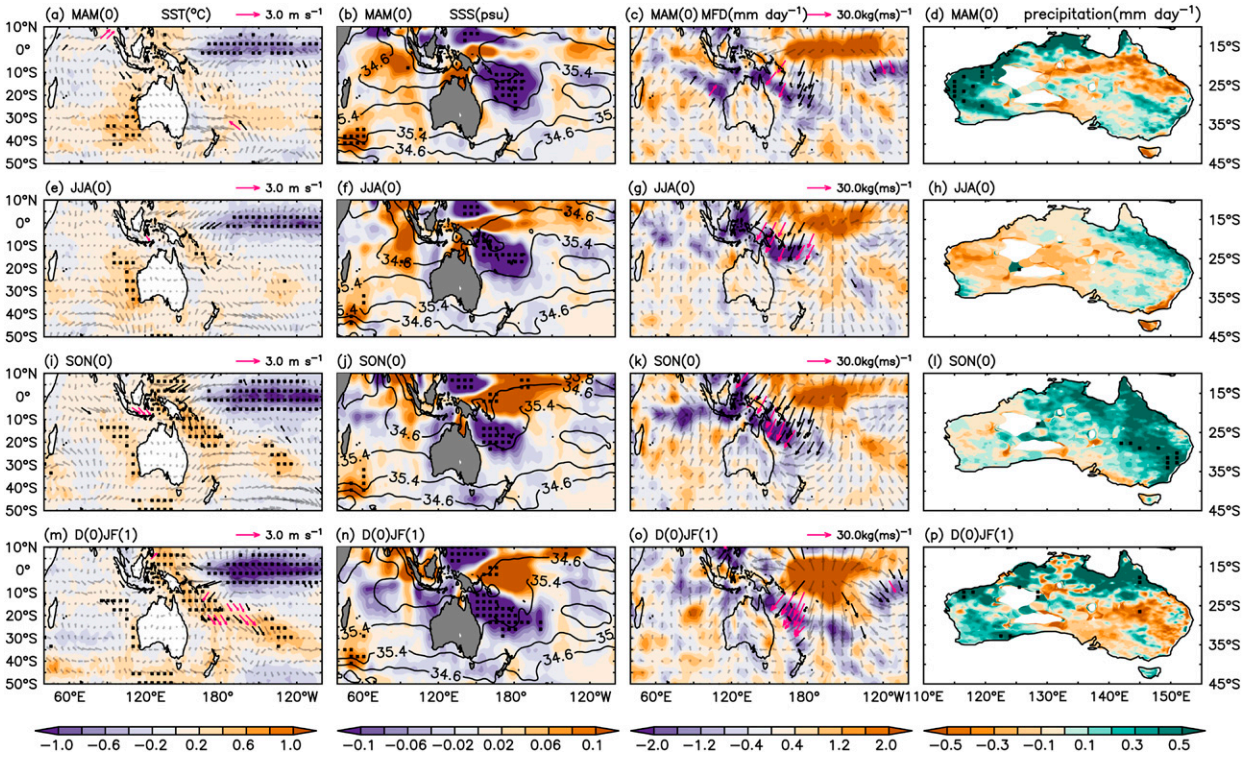

FIG. B2. Seasonal composite mean during pure La Niña of (a),(e),(i),(m) sea surface temperature anomaly (SST anomaly; shaded; °C) overlaid by 10-m anomalous surface winds (vectors; m s^{-1}), (b),(f),(j),(n) sea surface salinity anomaly (SSS anomaly; shaded; psu) overlaid by seasonal climatology of sea surface salinity (SSS; contour), (c),(g),(k),(o) moisture flux divergence anomaly (MFD; mm day^{-1}; shaded) overlaid by the divergent component of moisture flux anomaly (kg m^{-1} s^{-1}; vectors), and (d),(h),(l),(p) Australian precipitation anomaly (mm day^{-1}). Black dots indicate regions that are statistically significant at 95%, thick black vectors are statistically significant at 90%, and thick magenta vectors are statistically significant at 95% from Hotelling's *T*-square test.

minus precipitation) from the present generation reanalysis products, SSS appears to be an additional new variable to evaluate the $E - P$ field (Yu et al. 2017). However, our study does not account for the modification of upper-ocean salinity by oceanic processes (i.e., advection, diffusion, and vertical entrainment), as mentioned by Yu (2011), that are beyond the scope of the present study.

The use of satellites for monitoring SSS, evaporation, and precipitation on a global scale is also gaining attention. Satellite data from ESA/Soil Moisture and Ocean Salinity (SMOS) and Soil Moisture Active Passive (SMAP) missions reveal potential implications of monitoring SSS from space to understand the global hydrological cycle and the ocean circulation from the mesoscale through the gyre, basin, and global scales (Reul et al. 2014; Rast et al. 2014; Srokosz and Banks 2019). Moreover, recent studies show that SSS is a potential precursor for the prediction of ENSO and IOD events along with the terrestrial precipitation (Li et al. 2016a,b; J. Li et al. 2016; Hackert et al. 2019). The assimilation of SSS in the numerical model can improve the forecast of these events that eventually improve the forecast of terrestrial precipitation. Further analysis is required in this direction to use SSS to locate the oceanic sources of moisture for Australia that could aid rainfall prediction in varied climatic conditions. Therefore, we see the substantial utility in the continuous monitoring of the ocean surface and subsurface salinity through in situ and spaceborne measurements to understand Earth's hydrological cycle from global to regional scales.

10. Conclusions

This study investigates the ENSO and IOD impact on SSS, atmospheric moisture transport, and precipitation over Australia, and establishes the links among them. The link between SSS and Australian precipitation is further illustrated in the schematic of the extreme hydroclimatic conditions of Australia during 2010/11 austral summer (Fig. 8). Apart from the local recycling processes over the ocean surface, we show that the source of moisture transport from ocean to land can be identified by monitoring SSS. Importantly, the signature of anomalous positive SSS appears in the Indo-Pacific

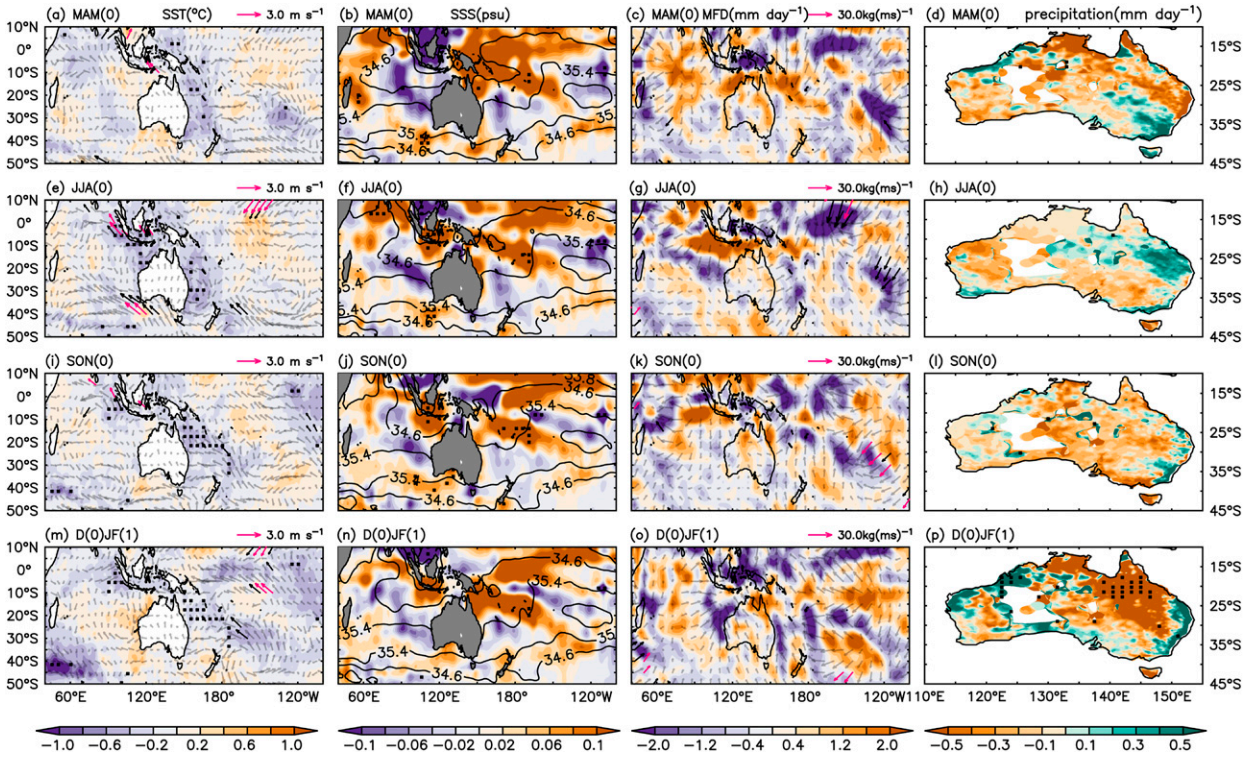

FIG. B3. Seasonal composite mean during pure pIOD of (a),(e),(i),(m) sea surface temperature anomaly (SST anomaly; shaded; °C) overlaid by 10-m anomalous surface winds (vectors; m s^{-1}), (b),(f),(j),(n) sea surface salinity anomaly (SSS anomaly; shaded; psu) overlaid by seasonal climatology of sea surface salinity (SSS; contour), (c),(g),(k),(o) moisture flux divergence anomaly (MFD; mm day^{-1}; shaded) overlaid by the divergent component of moisture flux anomaly (kg m^{-1} s^{-1}; vectors), and (d),(h),(l),(p) Australian precipitation anomaly (mm day^{-1}). Black dots indicate regions that are statistically significant at 95%, thick black vectors are statistically significant at 90%, and thick magenta vectors are statistically significant at 95% from Hotelling's *T*-square test.

warm pool region and over northern Australia prior to the monsoon rainfall season (DJF) (Figs. 4f,j, 5f,j, and 7f,j). Similarly, the mean moisture transport over the Australian continent is profoundly linked with the mean SSS in the Indo-Pacific basin (Fig. 3, columns 1, 2, and 3). Moreover, a large part of the mean monsoonal moisture that converges over Australia during DJF comes primarily from the Indian Ocean (Fig. 9j).

We show that with the evolution of ENSO and IOD events, a characteristic SSS anomaly signature in the Indo-Pacific Ocean emerges and is accompanied by moisture flux divergence anomalies. Moreover, the pattern correlation between SSS anomaly and moisture flux divergence progressively increases with the strengthening of the ENSO and IOD events. During co-occurring El Niño and pIOD events in DJF, anomalous dry conditions prevail over Australia (Fig. 4) due to the divergence of moisture flux. In contrast, during co-occurring La Niña and nIOD events, the Australian continent is anomalously wet with the convergence of moisture, particularly in the JJA, SON, and DJF periods (Fig. 5, column 3 and 4). When these co-occurring events peak, a maximum pattern correlation between MFD and SSS is observed (Fig. 6).

Finally, these results show that SSS variability is perhaps most directly linked with atmospheric moisture transport at seasonal and interannual time scales and at regional scales (Fig. 10). The long-term trends (on time scales of decades) in SSS that have been used for evidence of hydrological intensification are more complex because oceanic advection and mixing have a cumulative impact on SSS variability. However, the utility of SSS on regional spatial and temporal scales of months rather than decades, such as the case study of the extreme hydroclimatic event of the year 2010/11, exemplifies the scale separation nicely.

Acknowledgments. This research is funded through the Earth System and Climate Change Hub of the Australian government's National Environmental Science Programme. The assistance of computing resources from the National Computational Infrastructure supported by the Australian Government is acknowledged. CCU acknowledges support from the U.S. National Science

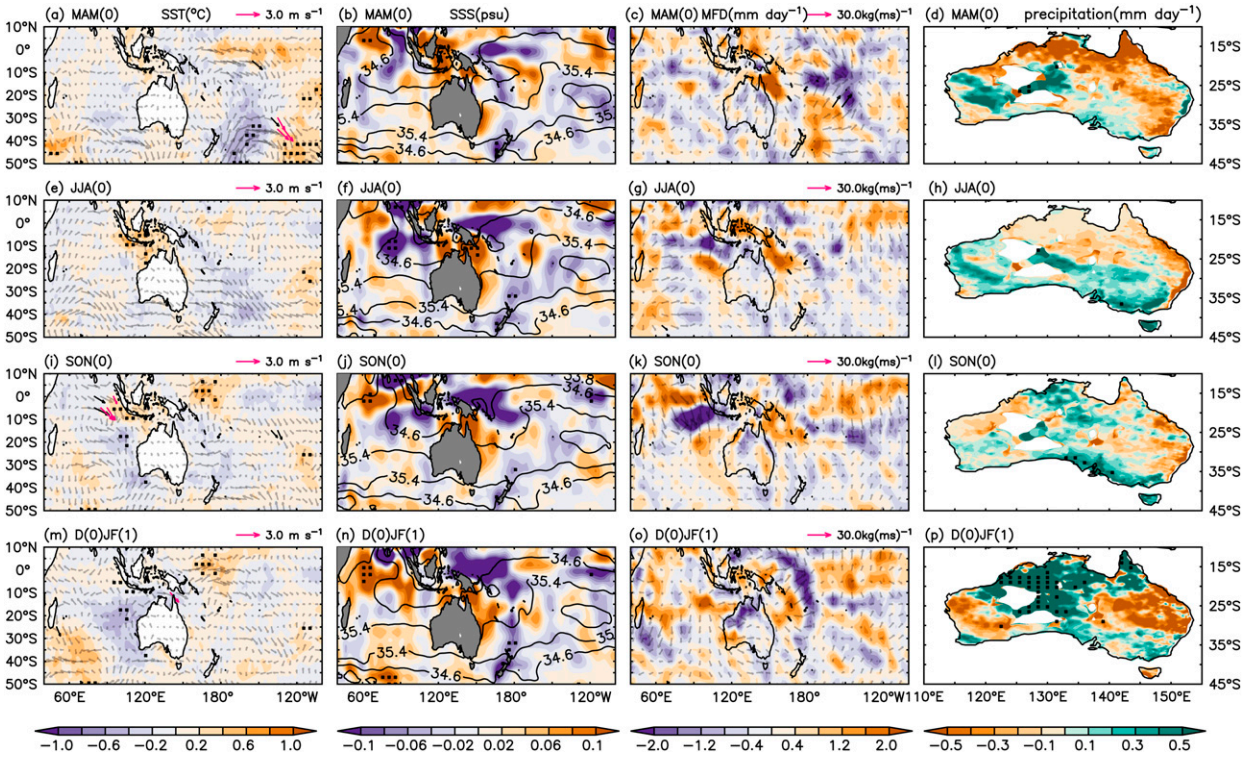

FIG. B4. Seasonal composite mean during pure nIOD of (a),(e),(i),(m) sea surface temperature anomaly (SST anomaly; shaded; °C) overlaid by 10-m anomalous surface winds (vectors; m s^{-1}), (b),(f),(j),(n) sea surface salinity anomaly (SSS anomaly; shaded; psu) overlaid by seasonal climatology of sea surface salinity (SSS; contour), (c),(g),(k),(o) moisture flux divergence anomaly (MFD; mm day^{-1}; shaded) overlaid by the divergent component of moisture flux anomaly (kg m^{-1} s^{-1}; vectors), and (d),(h),(l),(p) Australian precipitation anomaly (mm day^{-1}). Black dots indicate regions that are statistically significant at 95%, thick black vectors are statistically significant at 90%, and thick magenta vectors are statistically significant at 95% from Hotelling's *T*-square test.

Foundation under Grant OCE-1663704. MF was supported by the by Centre for Southern Hemisphere Oceans Research (CSHOR), which is a joint initiative between the Qingdao National Laboratory for Marine Science and Technology (QNLM), CSIRO, University of New South Wales and University of Tasmania. The authors wish to acknowledge PyFerret (https://ferret.pmel.noaa.gov/Ferret/) and the Cimate Data Operators (https://code.mpimet.mpg.de/projects/cdo/) for the data analysis and graphical representations in this paper. The authors thank four anonymous reviewers and the editor, whose comments significantly contributed to the improvement of this paper.

APPENDIX A

Hotelling's *T*-Square Test for Significance Testing of Composite Means

The term $X_{i,j}$ is the number of years chosen for ENSO and IOD events, here i represents season (MAM, JJA, SON, and DJF), and j represents the year of the event; $Y_{i,k}$ is the total number of years for seasonal average (i.e., $k = 57$ years for each ith season in our study); and μ_1 is the composite mean of $X_{i,j}$ (i.e., the composite mean of each season from the selected years of ENSO and IOD events). Let μ_2 be the seasonally average anomaly of $Y_{i,k}$ from all 57 years (i.e., the long-term seasonal mean).

The null hypothesis is H_0: $\mu_1 = \mu_2$ against the alternate hypothesis H_1: $\mu_1 \neq \mu_2$.

We are going to demonstrate the significance testing for co-occurring El Niño and pIOD cases during the MAM season as an example.

Here $X_{i,j}$ are the total number of each season for this event. We further denote this as $X_{\mathrm{MAM},j}$, where j represents years (1963/64, 1972/73, 1976/77, 1977/78, 1982/83, 1987/88, 1991/92, 1994/95, 1997/98, 2002/03, 2006/07, 2015/16).

$$\mu_1 = \frac{\sum_{j=1}^{j=n_{\mathrm{MAM}}} X_{\mathrm{MAM},j}}{n_{\mathrm{MAM}}},$$

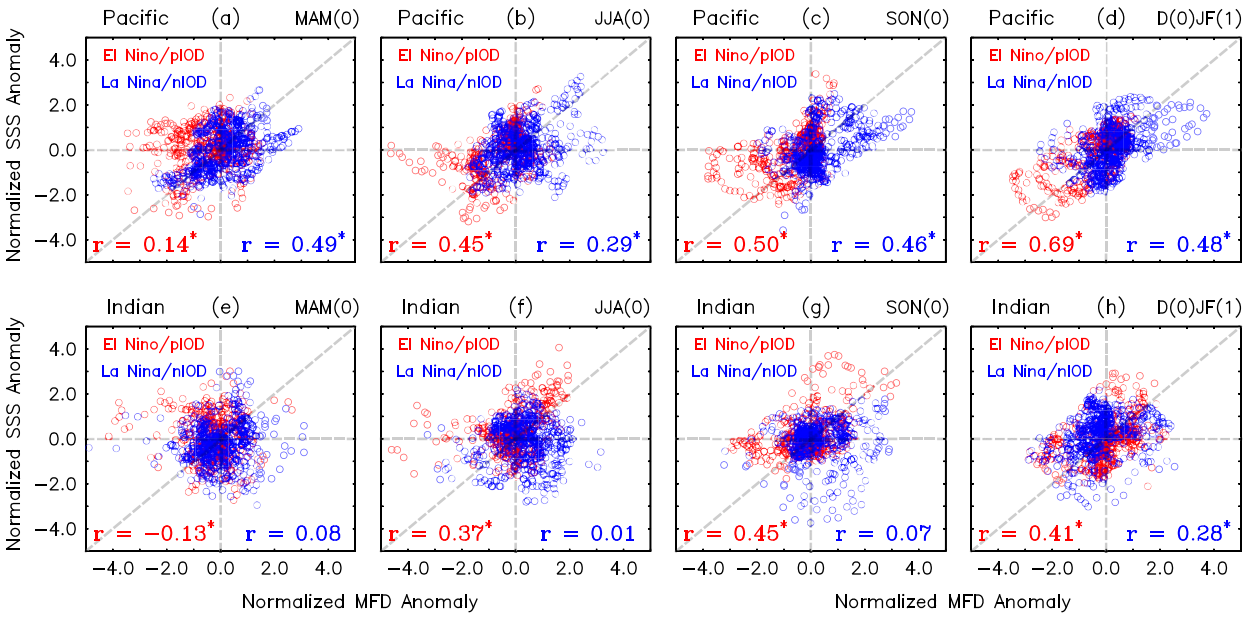

FIG. B5 . Pattern correlation analysis of seasonal composite mean of spatially normalized SSS anomaly (leading by 1 month) and MFD anomaly with their respective standard deviation during co-occurring El Niño and pIOD (red) and co-occurring La Niña and nIOD (blue) over (a)–(d) Pacific (150°E–150°W, 30°S–10°N) and (e)–(h) Indian Ocean (60°–120°E, 30°S–10°N). The pattern correlation coefficient r is shown at the bottom in all panels. The correlation coefficients that are statistically significant at 95% from a two-tailed Student's t test are marked with asterisks.

where $n_{\mathrm{MAM}} = 12$ (i.e., the number of MAM seasons during co-occurring El Niño and pIOD events).

$$\mu_2 = \frac{\sum_{k=1}^{k=57} Y_{\mathrm{MAM},k}}{57},$$

where $k = 57$ is the total number of years in our study.

$$S_x^2 = \frac{\sum_{j=1}^{j=n_{\mathrm{MAM}}} (X_{\mathrm{MAM},j} - \mu_1)^2}{n_{\mathrm{MAM}} - 1},$$

$$S_y^2 = \frac{\sum_{k=1}^{k=57} (Y_{\mathrm{MAM},k} - \mu_2)^2}{57 - 1},$$

w-

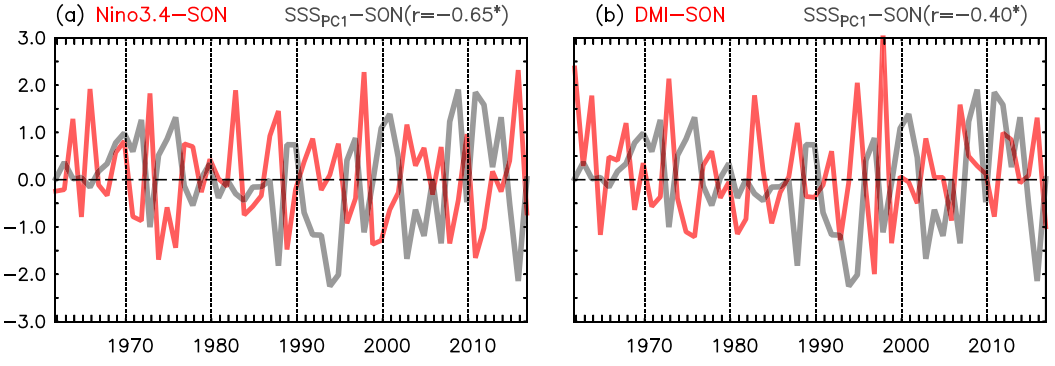

FIG. B6. Normalized time series of the Niño-3.4 index (red) and DMI (red) with the PC1 of SSS (gray) during SON with the correlation coefficient r in parentheses where the asterisk represents significance at 95% from a two-tailed Student's t test.

here S_x^2 and S_y^2 are the sample variances.

$$S_p^2 = \frac{(X_{n\mathrm{MAM}j} - 1)S_x^2 + (Y_{n\mathrm{MAM}k} - 1)S_y^2}{X_{n\mathrm{MAM}j} + Y_{n\mathrm{MAM}k} - 2},$$

where S_p^2 is the pooled variance, $X_{n\mathrm{MAM}j}$ is the number of MAM seasons for compositing during co-occurring El Niño and pIOD event (i.e., 12), and $Y_{n\mathrm{MAM}k}$ is the total number of MAM season in our study period (i.e., 57).

$$t = \frac{\mu_1 - \mu_1}{\sqrt{S_p^2\left(\frac{1}{X_{n\mathrm{MAM}j}} + \frac{1}{Y_{n\mathrm{MAM}k}}\right)}} \sim t_{X_{n\mathrm{MAM}j} + Y_{n\mathrm{MAM}k} - 2},$$

This test statistic will be t-distributed with $X_{n\mathrm{MAM}j} + Y_{n\mathrm{MAM}k} - 2$ degrees of freedom. The null hypothesis will be rejected if the test statistic "t" exceeds the critical value from the t table with $X_{n\mathrm{MAM}j} + Y_{n\mathrm{MAM}k} - 2$ at $\alpha/2$ significance level (i.e., $|t| > t_{X_{n\mathrm{MAM}j} + Y_{n\mathrm{MAM}k} - 2, \alpha/2}$).

APPENDIX B

Pure ENSO and IOD Events

Generally, IOD coincides with ENSO, which means pIOD is followed by El Niño, and nIOD is followed by La Niña; these sequences of events are known as co-occurring ENSO and IOD events. In the case of pure ENSO, there will be no signal of IOD in the Indian Ocean, but the Pacific Ocean exhibits a strong signal of ENSO. We also categorized our study based on co-occurring and pure events.

a. Pure El Niño and La Niña case

In our study, there are a total of 13 cases of pure ENSO in which seven events are pure El Niño (1965/66, 1969/70, 1979/80, 1986/87, 2004/05, 2009/10, and 2014/15) and six events are pure La Niña (1985/86, 1988/89, 1995/96, 1999/2000, 2000/01, and 2008/09) The selection of these events is based on the threshold criteria, as described in the methods section (section 2b).

The pure El Niño events (Fig. B1) are markedly different from the co-occurring El Niño and pIOD events in terms of strength of salinity and moisture transport. The salinity and moisture transport signals during pure ENSO events are relatively weak as compared to co-occurring ENSO and IOD events.

During pure El Niño events in DJF (Fig. B1), the Australian continent is not as dry as it is during co-occurring El Niño and pIOD events (Fig. 4). Similarly, in the case of pure La Niña events (Fig. B2) during SON, the Australian continent is not as wet as it is in co-occurring La Niña and nIOD events (Fig. 5). Moreover, during DJF, the pattern of precipitation over Australia during pure La Niña events is more toward the eastern half from north to south Australia. Whereas, during co-occurring La Niña and nIOD events, the Australian precipitation is more on the east-west coast of Australia.

b. Pure pIOD/nIOD case

In our study, there are seven cases of pure IOD events from the selection criteria described in the methods section (section 2b). Out of 7 events of pure IOD, three are pure pIOD (1961, 1966, and 2012), and four are nIOD cases (1980, 1981, 1992, and 2001).

The cases of pure pIOD (Fig. B3) and nIOD (Fig. B4) events show relatively weak signals of salinity and moisture transport as compared to pure ENSO and co-occurring ENSO and IOD events. This suggests the relative importance of ENSO events as compared to IOD events to modulate oceanic and atmospheric fields. During pure pIOD (nIOD), southeast Australia in SON is anomalously dry (wet). Similarly, during the pIOD event in DJF northern (eastern) Australia is anomalously dry (wet), and vice versa for the nIOD event.

The pattern correlation of the seasonal composite mean of normalized SSS anomaly leading by 1 month and the MFD anomaly during co-occurring El Niño/pIOD and co-occurring La Niña/nIOD is shown in Fig. B5. The normalized time series of the Niño-3.4 index and dipole mode index with PC1 of SSS during SON is shown in Fig. B6.

REFERENCES

Allan, R., and Coauthors, 2001: Is there an equatorial Indian Ocean SST dipole independent of the El Niño–Southern Oscillation? *CLIVAR Exchanges*, No. 6, International CLIVAR Project Office, Southampton, United Kingdom, 18–22, http://eprints.uni-kiel.de/13692/1/Exchanges21.pdf.

Ashok, K., Z. Guan, and T. Yamagata, 2003: Influence of the Indian Ocean dipole on the Australian winter rainfall. *Geophys. Res. Lett.*, **30**, 1821, https://doi.org/10.1029/2003GL017926.

Ballabrera-Poy, J., R. Murtugudde, and A. J. Busalacchi, 2002: On the potential impact of sea surface salinity observations on ENSO predictions. *J. Geophys. Res.*, **107**, 8007, https://doi.org/10.1029/2001JC000834.

Balmaseda, M. A., K. E. Trenberth, and E. Källén, 2013: Distinctive climate signals in reanalysis of global ocean heat content. *Geophys. Res. Lett.*, **40**, 1754–1759, https://doi.org/10.1002/grl.50382.

Bindoff, N. L., and Coauthors, 2013: Detection and attribution of climate change: From global to regional. *Climate Change 2013: The Physical Science Basis*, T. F. Stocker et al., Eds., Cambridge University Press, 867–952.

Boening, C., J. K. Willis, F. W. Landerer, R. S. Nerem, and J. Fasullo, 2012: The 2011 La Niña: So strong, the oceans fell. *Geophys. Res. Lett.*, **39**, L19602, https://doi.org/10.1029/2012GL053055.

Bowen, G. J., 2011: A faster water cycle. *Science*, **332**, 430–431, https://doi.org/10.1126/science.1205253.

Brown, J. N., P. C. McIntosh, M. J. Pook, and J. S. Risbey, 2009: An investigation of the links between ENSO flavors and rainfall processes in southeastern Australia. *Mon. Wea. Rev.*, **137**, 3786–3795, https://doi.org/10.1175/2009MWR3066.1.

Cai, W., T. Cowan, and A. Sullivan, 2009: Recent unprecedented skewness towards positive Indian Ocean Dipole occurrences and its impact on Australian rainfall. *Geophys. Res. Lett.*, **36**, L11705, https://doi.org/10.1029/2009GL037604.

——, P. van Rensch, T. Cowan, and H. H. Hendon, 2011: Teleconnection pathways of ENSO and the IOD and the mechanisms for impacts on Australian rainfall. *J. Climate*, **24**, 3910–3923, https://doi.org/10.1175/2011JCLI4129.1.

——, ——, ——, and ——, 2012: An asymmetry in the IOD and ENSO teleconnection pathway and its impact on Australian climate. *J. Climate*, **25**, 6318–6329, https://doi.org/10.1175/JCLI-D-11-00501.1.

Chen, B., H. Qin, G. Chen, and H. Xue, 2019: Ocean salinity as a precursor of summer rainfall over the East Asian monsoon region. *J. Climate*, **32**, 5659–5676, https://doi.org/10.1175/JCLI-D-18-0756.1.

Decker, M., A. Pitman, and J. Evans, 2015: Diagnosing the seasonal land–atmosphere correspondence over northern Australia: Dependence on soil moisture state and correspondence strength definition. *Hydrol. Earth Syst. Sci.*, **19**, 3433–3447, https://doi.org/10.5194/hess-19-3433-2015.

Dee, D. P., and Coauthors, 2011: The ERA-Interim reanalysis: Configuration and performance of the data assimilation system. *Quart. J. Roy. Meteor. Soc.*, **137**, 553–597, https://doi.org/10.1002/qj.828.

Durack, P. J., S. E. Wijffels, and R. J. Matear, 2012: Ocean salinities reveal strong global water cycle intensification during 1950 to 2000. *Science*, **336**, 455–458, https://doi.org/10.1126/science.1212222.

Evans, J. P., and I. Boyer-Souchet, 2012: Local sea surface temperatures add to extreme precipitation in northeast Australia during La Niña. *Geophys. Res. Lett.*, **39**, L10803, https://doi.org/10.1029/2012GL052014.

——, A. J. Pitman, and F. T. Cruz, 2011: Coupled atmospheric and land surface dynamics over southeast Australia: A review, analysis and identification of future research priorities. *Int. J. Climatol.*, **31**, 1758–1772, https://doi.org/10.1002/joc.2206.

——, X. Meng, and M. F. McCabe, 2017: Land surface albedo and vegetation feedbacks enhanced the millennium drought in south-east Australia. *Hydrol. Earth Syst. Sci.*, **21**, 409–422, https://doi.org/10.5194/hess-21-409-2017.

Fasullo, J. T., C. Boening, F. W. Landerer, and R. S. Nerem, 2013: Australia's unique influence on global sea level in 2010–2011. *Geophys. Res. Lett.*, **40**, 4368–4373, https://doi.org/10.1002/grl.50834.

Feng, H., and M. Zhang, 2016: Global land moisture trends: Drier in dry and wetter in wet over land. *Sci. Rep.*, **5**, 18018, https://doi.org/10.1038/srep18018.

Feng, M., M. J. McPhaden, S.-P. Xie, and J. Hafner, 2013: La Niña forces unprecedented Leeuwin Current warming in 2011. *Sci. Rep.*, **3**, 1277, https://doi.org/10.1038/srep01277.

——, J. Benthuysen, N. Zhang, and D. Slawinski, 2015: Freshening anomalies in the Indonesian Throughflow and impacts on the Leeuwin Current during 2010–2011. *Geophys. Res. Lett.*, **42**, 8555–8562, https://doi.org/10.1002/2015GL065848.

Good, S. A., M. J. Martin, and N. A. Rayner, 2013: EN4: Quality controlled ocean temperature and salinity profiles and monthly objective analyses with uncertainty estimates. *J. Geophys. Res. Oceans*, **118**, 6704–6716, https://doi.org/10.1002/2013JC009067.

Gouretski, V., and F. Reseghetti, 2010: On depth and temperature biases in bathythermograph data: Development of a new correction scheme based on analysis of a global ocean database. *Deep-Sea Res. I*, **57**, 812–833, https://doi.org/10.1016/J.DSR.2010.03.011.

Greve, P., B. Orlowsky, B. Mueller, J. Sheffield, M. Reichstein, and S. I. Seneviratne, 2014: Global assessment of trends in wetting and drying over land. *Nat. Geosci.*, **7**, 716–721, https://doi.org/10.1038/ngeo2247.

Hackert, E., J. Ballabrera-Poy, A. J. Busalacchi, R.-H. Zhang, and R. Murtugudde, 2011: Impact of sea surface salinity assimilation on coupled forecasts in the tropical Pacific. *J. Geophys. Res.*, **116**, C05009, https://doi.org/10.1029/2010JC006708.

——, R. M. Kovach, A. J. Busalacchi, and J. Ballabrera-Poy, 2019: Impact of Aquarius and SMAP satellite sea surface salinity observations on coupled El Niño/Southern Oscillation forecasts. *J. Geophys. Res. Oceans*, **124**, 4546–4556, https://doi.org/10.1029/2019JC015130.

Hayes, J., and A. Goonetilleke, 2013: Building community resilience – Learning from the 2011 floods in Southeast Queensland, Australia. *Proc. Eighth Annual Conf. of International Institute Infrastructure, Renewal and Reconstruction (IIIRR 2012) International Conf. on Disaster Management (IIIRR 2012)*, Kumamoto University, Kumamoto, 51–60.

Helm, K. P., N. L. Bindoff, and J. A. Church, 2010: Changes in the global hydrological-cycle inferred from ocean salinity. *Geophys. Res. Lett.*, **37**, L18701, https://doi.org/10.1029/2010GL044222.

Holgate, C. M., A. I. J. M. Van Dijk, J. P. Evans, and A. J. Pitman, 2019: The importance of the one-dimensional assumption in soil moisture–rainfall depth correlation at varying spatial scales. *J. Geophys. Res. Atmos.*, **124**, 2964–2975, https://doi.org/10.1029/2018JD029762.

Holmes, C., 2012: Final report. Queensland Floods Commission of Inquiry, 658 pp., http://www.floodcommission.qld.gov.au/publications/final-report/.

Hong, C.-C., T. Li, LinHo, and Y.-C Chen, 2010: Asymmetry of the Indian Ocean basinwide SST anomalies: Roles of ENSO and IOD. *J. Climate*, **23**, 3563–3576, https://doi.org/10.1175/2010JCLI3320.1.

Hosoda, S., T. Suga, N. Shikama, and K. Mizuno, 2009: Global surface layer salinity change detected by Argo and its implication for hydrological cycle intensification. *J. Oceanogr.*, **65**, 579–586, https://doi.org/10.1007/s10872-009-0049-1.

Hotelling, H., 1931: The generalization of Student's ratio. *Ann. Math. Stat.*, **2**, 360–378, https://doi.org/10.1214/aoms/1177732979.

Huang, B., and Coauthors, 2017: Extended Reconstructed Sea Surface Temperature, version 5 (ERSSTv5): Upgrades, validations, and intercomparisons. *J. Climate*, **30**, 8179–8205, https://doi.org/10.1175/JCLI-D-16-0836.1.

Huntington, T. G., 2006: Evidence for intensification of the global water cycle: Review and synthesis. *J. Hydrol.*, **319**, 83–95, https://doi.org/10.1016/j.jhydrol.2005.07.003.

Jansen, M. F., D. Dommenget, and N. Keenlyside, 2009: Tropical atmosphere–ocean interactions in a conceptual framework. *J. Climate*, **22**, 550–567, https://doi.org/10.1175/2008JCLI2243.1.

Kalnay, E., and Coauthors, 1996: The NCEP/NCAR 40-Year Reanalysis Project. *Bull. Amer. Meteor. Soc.*, **77**, 437–471, https://doi.org/10.1175/1520-0477(1996)077<0437:TNYRP>2.0.CO;2.

Kataoka, T., T. Tozuka, S. Behera, and T. Yamagata, 2014: On the Ningaloo Niño/Niña. *Climate Dyn.*, **43**, 1463–1482, https://doi.org/10.1007/s00382-013-1961-z.

Kido, S., and T. Tozuka, 2017: Salinity variability associated with the positive Indian Ocean dipole and its impact on the upper ocean temperature. *J. Climate*, **30**, 7885–7907, https://doi.org/10.1175/JCLI-D-17-0133.1.

——, ——, and W. Han, 2019: Anatomy of salinity anomalies associated with the positive Indian Ocean Dipole. *J. Geophys. Res. Oceans*, **124**, 8116–8139, https://doi.org/10.1029/2019JC015163.

King, A. D., M. G. Donat, L. V. Alexander, and D. J. Karoly, 2015: The ENSO–Australian rainfall teleconnection in reanalysis and CMIP5. *Climate Dyn.*, **44**, 2623–2635, https://doi.org/10.1007/s00382-014-2159-8.

Koul, V., A. Parekh, G. Srinivas, R. Kakatkar, J. S. Chowdary, and C. Gnanaseelan, 2018: Role of ocean initial conditions to diminish dry bias in the seasonal prediction of Indian summer monsoon rainfall: A case study using climate forecast system. *J. Adv. Model. Earth Syst.*, **10**, 603–616, https://doi.org/10.1002/2017MS001129.

Kumar, S., R. P. Allan, F. Zwiers, D. M. Lawrence, and P. A. Dirmeyer, 2015: Revisiting trends in wetness and dryness in the presence of internal climate variability and water limitations over land. *Geophys. Res. Lett.*, **42**, 10 867–10 875, https://doi.org/10.1002/2015GL066858.

Lestari, R. K., and T. Y. Koh, 2016: Statistical evidence for asymmetry in ENSO–IOD interactions. *Atmos.–Ocean*, **54**, 498–504, https://doi.org/10.1080/07055900.2016.1211084.

Li, J., C. Liang, Y. Tang, C. Dong, D. Chen, X. Liu, and W. Jin, 2016: A new dipole index of the salinity anomalies of the tropical Indian Ocean. *Sci. Rep.*, **6**, 24260, https://doi.org/10.1038/srep24260.

Li, L., W. Li, and A. P. Barros, 2013: Atmospheric moisture budget and its regulation of the summer precipitation variability over the southeastern United States. *Climate Dyn.*, **41**, 613–631, https://doi.org/10.1007/s00382-013-1697-9.

——, R. W. Schmitt, C. C. Ummenhofer, and K. B. Karnauskas, 2016a: North Atlantic salinity as a predictor of Sahel rainfall. *Sci. Adv.*, **2**, e1501588, https://doi.org/10.1126/sciadv.1501588.

——, ——, ——, and ——, 2016b: Implications of North Atlantic sea surface salinity for summer precipitation over the U.S. Midwest: Mechanisms and predictive value. *J. Climate*, **29**, 3143–3159, https://doi.org/10.1175/JCLI-D-15-0520.1.

Lim, E. P., and H. H. Hendon, 2015: Understanding and predicting the strong southern annular mode and its impact on the record wet east Australian spring 2010. *Climate Dyn.*, **44**, 2807–2824, https://doi.org/10.1007/s00382-014-2400-5.

——, ——, J. M. Arblaster, C. Chung, A. F. Moise, P. Hope, G. Young, and M. Zhao, 2016: Interaction of the recent 50 year SST trend and La Niña 2010: Amplification of the southern annular mode and Australian springtime rainfall. *Climate Dyn.*, **47**, 2273–2291, https://doi.org/10.1007/s00382-015-2963-9.

Lynch, P., 1988: Deducing the wind from vorticity and divergence. *Mon. Wea. Rev.*, **116**, 86–93, https://doi.org/10.1175/1520-0493(1988)116<0086:DTWFVA>2.0.CO;2.

McBride, J. L., and N. Nicholls, 1983: Seasonal relationships between Australian rainfall and the Southern Oscillation. *Mon. Wea. Rev.*, **111**, 1998–2004, https://doi.org/10.1175/1520-0493(1983)111<1998:SRBARA>2.0.CO;2.

Meyers, G., P. McIntosh, L. Pigot, and M. Pook, 2007: The years of El Niño, La Niña, and interactions with the tropical Indian Ocean. *J. Climate*, **20**, 2872–2880, https://doi.org/10.1175/JCLI4152.1.

NCCARF, 2011: Protecting structures from floodwater. National Climate Change Adaptation Research Facility, 2 pp., https://www.nccarf.edu.au/sites/default/files/attached_files_publications/ProtectingStructuresfromFloodwater-factsheet_0.pdf.

New, M., M. Hulme, and P. Jones, 2000: Representing twentieth-century space–time climate variability. Part II: Development of 1901–96 monthly grids of terrestrial surface climate. *J. Climate*, **13**, 2217–2238, https://doi.org/10.1175/1520-0442(2000)013<2217:RTCSTC>2.0.CO;2.

Pearce, A. F., and M. Feng, 2013: The rise and fall of the ''marine heat wave'' off Western Australia during the summer of 2010/2011. *J. Mar. Syst.*, **111–112**, 139–156, https://doi.org/10.1016/j.jmarsys.2012.10.009.

Pepler, A., B. Timbal, C. Rakich, and A. Coutts-Smith, 2014: Indian Ocean dipole overrides ENSO's influence on cool season rainfall across the eastern seaboard of Australia. *J. Climate*, **27**, 3816–3826, https://doi.org/10.1175/JCLI-D-13-00554.1.

Polson, D., and G. C. Hegerl, 2017: Strengthening contrast between precipitation in tropical wet and dry regions. *Geophys. Res. Lett.*, **44**, 365–373, https://doi.org/10.1002/2016GL071194.

Queenland Government, 2015: 2010–11 flood impacts. accessed 13 May 2019, https://www.qld.gov.au/environment/pollution/management/disasters/flood-impacts.

Rast, M., J. Johannessen, and W. Mauser, 2014: Review of understanding of Earth's hydrological cycle: Observations, theory and modelling. *Surv. Geophys.*, **35**, 491–513, https://doi.org/10.1007/s10712-014-9279-x.

Raupach, M. R., P. R. Briggs, V. Haverd, E. A. King, M. Paget, and C. M. Trudinger, 2009: Australian Water Availability Project (AWAP): CSIRO marine and atmospheric research component: Final report for phase 3. CAWCR Tech. Rep. 13, 67 pp.

Raval, A., and V. Ramanathan, 1989: Observational determination of the greenhouse effect. *Nature*, **342**, 758–761, https://doi.org/10.1038/342758a0.

Rayner, N. A., D. E. Parker, E. B. Horton, C. K. Folland, L. V. Alexander, D. P. Rowell, E. C. Kent, and A. Kaplan, 2003: Global analyses of sea surface temperature, sea ice, and night marine air temperature since the late nineteenth century. *J. Geophys. Res.*, **108**, 4407, https://doi.org/10.1029/2002JD002670.

Reul, N., and Coauthors, 2014: Sea surface salinity observations from space with the SMOS satellite: A new means to monitor the marine branch of the water cycle. *Surv. Geophys.*, **35**, 681–722, https://doi.org/10.1007/s10712-013-9244-0.

Risbey, J. S., M. J. Pook, P. C. McIntosh, M. C. Wheeler, and H. H. Hendon, 2009: On the remote drivers of rainfall variability in Australia. *Mon. Wea. Rev.*, **137**, 3233–3253, https://doi.org/10.1175/2009MWR2861.1.

Saji, N. H., and T. Yamagata, 2003: Possible impacts of Indian Ocean Dipole mode events on global climate. *Climate Res.*, **25**, 151–169, https://doi.org/10.3354/cr025151.

——, B. N. Goswami, P. N. Vinayachandran, and T. Yamagata, 1999: A dipole mode in the tropical Indian Ocean. *Nature*, **401**, 360–363, https://doi.org/10.1038/43854.

Santoso, A., M. J. Mcphaden, and W. Cai, 2017: The defining characteristics of ENSO extremes and the strong 2015/2016 El Niño. *Rev. Geophys.*, **55**, 1079–1129, https://doi.org/10.1002/2017RG000560.

Seager, R., and N. Henderson, 2013: Diagnostic computation of moisture budgets in the ERA-Interim reanalysis with reference to analysis of CMIP-archived atmospheric model data. *J. Climate*, **26**, 7876–7901, https://doi.org/10.1175/JCLI-D-13-00018.1.

Seelanki, V., P. Sreenivas, and K. V. S. R. Prasad, 2018: Impact of Aquarius sea-surface salinity assimilation in improving the ocean analysis over Indian Ocean. *Mar. Geod.*, **41**, 144–158, https://doi.org/10.1080/01490419.2017.1422817.

Singh, A., and T. Delcroix, 2011: Estimating the effects of ENSO upon the observed freshening trends of the western tropical Pacific Ocean. *Geophys. Res. Lett.*, **38**, L21607, https://doi.org/10.1029/2011GL049636.

Srokosz, M., and C. Banks, 2019: Salinity from space. *Weather*, **74**, 3–8, https://doi.org/10.1002/wea.3161.

Stuecker, M. F., A. Timmermann, F.-F. Jin, Y. Chikamoto, W. Zhang, A. T. Wittenberg, E. Widiasih, and S. Zhao, 2017: Revisiting ENSO/Indian Ocean dipole phase relationships. *Geophys. Res. Lett.*, **44**, 2481–2492, https://doi.org/10.1002/2016GL072308.

Sun, Q., Y. Du, Y. Zhang, M. Feng, J. S. Chowdary, J. Chi, S. Qiu, and W. Yu, 2019: Evolution of sea surface salinity anomalies in the southwestern tropical Indian Ocean during 2010–2011 influenced by a negative IOD event. *J. Geophys. Res. Oceans*, **124**, 3428–3445, https://doi.org/10.1029/2018JC014580.

Taschetto, A. S., A. Sen Gupta, H. H. Hendon, C. C. Ummenhofer, and M. H. England, 2011: The contribution of Indian Ocean sea surface temperature anomalies on Australian summer rainfall during El Niño events. *J. Climate*, **24**, 3734–3747, https://doi.org/10.1175/2011JCLI3885.1.

Trenberth, K. E., 2011: Changes in precipitation with climate change. *Climate Res.*, **47**, 123–138, https://doi.org/10.3354/cr00953.

Ummenhofer, C. C., M. H. England, P. C. Mclntosh, G. A. Meyers, M. J. Pook, J. S. Risbey, A. Sen Gupta, and A. S. Taschetto, 2009: What causes southeast Australia's worst droughts? *Geophys. Res. Lett.*, **36**, L04706, https://doi.org/10.1029/2008GL036801.

——, and Coauthors, 2011: Indian and Pacific Ocean influences on southeast Australian drought and soil moisture. *J. Climate*, **24**, 1313–1336, https://doi.org/10.1175/2010JCLI3475.1.

——, A. Sen Gupta, M. H. England, A. S. Taschetto, P. R. Briggs, and M. R. Raupach, 2015: How did ocean warming affect Australian rainfall extremes during the 2010/2011 La Niña event? *Geophys. Res. Lett.*, **42**, 9942–9951, https://doi.org/10.1002/2015GL065948.

Yaremchuk, M., 2006: Sea surface salinity constrains rainfall estimates over tropical oceans. *Geophys. Res. Lett.*, **33**, L15605, https://doi.org/10.1029/2006GL026582.

Yu, L., 2011: A global relationship between the ocean water cycle and near-surface salinity. *J. Geophys. Res.*, **116**, C10025, https://doi.org/10.1029/2010JC006937.

——, X. Jin, S. A. Josey, T. Lee, A. Kumar, C. Wen, and Y. Xue, 2017: The global ocean water cycle in atmospheric reanalysis, satellite, and ocean salinity. *J. Climate*, **30**, 3829–3852, https://doi.org/10.1175/JCLI-D-16-0479.1.

Zhao, M., H. H. Hendon, Y. Yin, and O. Alves, 2016: Variations of upper-ocean salinity associated with ENSO from PEODAS reanalyses. *J. Climate*, **29**, 2077–2094, https://doi.org/10.1175/JCLI-D-15-0650.1.

——, H. Zhang, and I. Dharssi, 2019: On the soil moisture memory and influence on coupled seasonal forecasts over Australia. *Climate Dyn.*, **52**, 7085–7109, https://doi.org/10.1007/s00382-018-4566-8.

Zhi, H., R. H. Zhang, P. Lin, and S. Shi, 2019: Effects of salinity variability on recent El Niño events. *Atmosphere*, **10**, 475, https://doi.org/10.3390/ATMOS10080475.

Zhou, T. J., and R. C. Yu, 2005: Atmospheric water vapor transport associated with typical anomalous summer rainfall patterns in China. *J. Geophys. Res.*, **110**, D08104, https://doi.org/10.1029/2004JD005413.

Zhu, J., B. Huang, R. H. Zhang, Z. Z. Hu, A. Kumar, M. A. Balmaseda, L. Marx, and J. L. Kinter, 2014: Salinity anomaly as a trigger for ENSO events. *Sci. Rep.*, **4**, 6821, https://doi.org/10.1038/SREP06821.